Infrasound Radiation from Impulsive Volcanic Eruptions: Nonlinear Aeroacoustic 2D Simulations

Leighton M Watson[1,1], Eric M Dunham[2,2], Danyal Mohaddes[2,2], Jeff Labahn[2,2], Thomas Jaravel[3,3], and Matthias Ihme[2,2]

[1]University of Oregon
[2]Stanford University
[3]CERFACS

November 30, 2022

Abstract

Infrasound observations are increasingly used to constrain properties of volcanic eruptions. In order to better interpret infrasound observations, however, there is a need to better understand the relationship between eruption properties and sound generation. Here we perform two-dimensional computational aeroacoustic simulations where we solve the compressible Navier-Stokes equations for pure-air with a large-eddy simulation approximation. We simulate idealized impulsive volcanic eruptions where the exit velocity is specified and the eruption is pressure-balanced with the atmosphere. Our nonlinear simulation results are compared with the commonly-used analytical linear acoustics model of a compact monopole source radiating acoustic waves isotropically in a half space. The monopole source model matches the simulations for low exit velocities (<100 m/s or M ˜ 0.3 where M is the Mach number); however, the two solutions diverge as the exit velocity increases with the simulations developing lower peak amplitude, more rapid onset, and anisotropic radiation with stronger infrasound signals recorded above the vent than on Earth's surface. Our simulations show that interpreting ground-based infrasound observations with the monopole source model can result in an underestimation of the erupted volume for eruptions with sonic or supersonic exit velocities. We examine nonlinear effects and show that nonlinear effects during propagation are relatively minor for the parameters considered. Instead, the dominant nonlinear effect is advection by the complex flow structure that develops above the vent. This work demonstrates the need to consider anisotropic radiation patterns and jet dynamics when interpreting infrasound observations, particularly for eruptions with sonic or supersonic exit velocities.

Infrasound Radiation from Impulsive Volcanic Eruptions: Nonlinear Aeroacoustic 2D Simulations

Leighton M. Watson[1,2], Eric M. Dunham[2,3], Danyal Mohaddes[4], Jeff Labahn[5], Thomas Jaravel[5], Matthias Ihme[4]

[1]Department of Earth Sciences, University of Oregon, Eugene, Oregon, 97403, USA
[2]Department of Geophysics, Stanford University, Stanford, California, 94305, USA
[3]Institute of Computational and Mathematical Engineering, Stanford University, Stanford, California, 94305, USA
[4]Department of Mechanical Engineering, Stanford University, Stanford, California, 94305, USA
[5]Center for Turbulence Research, Stanford University, Stanford, California, 94305, USA

Key Points:

- Aeroacoustic simulations from the start-up of a pressure-balanced volcanic jet model fluid flow and infrasound radiation
- Compact monopole source model underpredicts the erupted volume for eruptions with sonic or supersonic exit velocities
- Infrasound radiation pattern depends on jet dynamics and is highly anisotropic for eruptions with sonic or supersonic exit velocities

Corresponding author: Leighton M. Watson, `lwatson2@uoregon.edu`

Abstract

Infrasound observations are increasingly used to constrain properties of volcanic eruptions. In order to better interpret infrasound observations, however, there is a need to better understand the relationship between eruption properties and sound generation. Here we perform two-dimensional computational aeroacoustic simulations where we solve the compressible Navier-Stokes equations for pure-air with a large-eddy simulation approximation. We simulate idealized impulsive volcanic eruptions where the exit velocity is specified and the eruption is pressure-balanced with the atmosphere. Our nonlinear simulation results are compared with the commonly-used analytical linear acoustics model of a compact monopole source radiating acoustic waves isotropically in a half space. The monopole source model matches the simulations for low exit velocities (up to 100 m/s or $M \approx 0.3$ where M is the Mach number); however, the two solutions diverge as the exit velocity increases with the simulations developing lower peak amplitude, more rapid onset, and anisotropic radiation with stronger infrasound signals recorded above the vent than on Earth's surface. Our simulations show that interpreting ground-based infrasound observations with the monopole source model can result in an underestimation of the erupted volume for eruptions with sonic or supersonic exit velocities. We examine nonlinear effects and show that nonlinear effects during propagation are relatively minor for the parameters considered. Instead, the dominant nonlinear effect is advection by the complex flow structure that develops above the vent. This work demonstrates the need to consider anisotropic radiation patterns and jet dynamics when interpreting infrasound observations, particularly for eruptions with sonic or supersonic exit velocities.

Plain Language Summary

Volcanic eruptions are noisy phenomena. During an eruption material is thrown into the atmosphere, pushing air out of the way and generating low frequency sound waves termed infrasound. We use infrasound observations to learn about the properties of volcanic eruptions. However, our understanding of the complex processes that generate sound during a volcanic eruption is limited. In order to address this, we perform simulations of volcanic eruptions and the associated infrasound signal. We compare our simulation results to an analytical model that is commonly used to interpret volcano infrasound observation. We show that for low exit velocities (up to 100 m/s or $M \approx 0.3$ where M is the Mach number) the analytical model does a good job in explaining the infrasound observations and the radiation pattern. However, for higher exit velocities the analytical model overpredicts the peak amplitude of the infrasound signal, underpredicts the erupted volume, and does not account for the directionality of the radiation pattern. This work quantifies some of the complexities that should be considered when interpreting infrasound observations and is a step towards developing more sophisticated source models for volcanic eruptions.

1 Introduction

During a volcanic eruption material is ejected from the volcano into the atmosphere and the eruptive fluid interacts with the atmospheric air to form a jet. The displacement and compression of the atmospheric air by the expansion of the jet generates acoustic waves, which are predominantly at low frequencies (< 20 Hz) and are termed infrasound (Johnson & Ripepe, 2011; Fee & Matoza, 2013; Garces et al., 2013; Marchetti et al., 2019; Matoza et al., 2019). Infrasound observations are increasingly used to detect and monitor volcanic activity (Arnoult et al., 2010; Coombs et al., 2018; Ripepe et al., 2018; De Angelis et al., 2019) as well as to constrain eruption properties including eruptive volume and mass (Johnson & Miller, 2014; Kim et al., 2015; Fee et al., 2017; Iezzi et al., 2019), plume height (Caplan-Auerbach et al., 2010; Lamb et al., 2015; Yamada et al., 2017; Perttu et al., 2020), and crater dimensions (Fee et al., 2010; Richardson et al., 2014; Johnson et al., 2018; Witsil & Johnson, 2018; Watson et al., 2019, 2020). Infrasound signals can propagate great distances in the atmosphere and can be used for regional (15 - 250 km) and remote (> 250 km) detection and characterization of eruptions (Fee & Matoza, 2013; Matoza et al., 2019; Marchetti et al., 2019). In this work, however, we focus on local ($<$ 15 km) infrasound.

The majority of volcano infrasound studies assume compact (i.e., point) sources, linear wave propagation, and do not account for fluid flow in the complex region near the vent. These simplifying assumptions have been extremely useful for interpreting volcano infrasound signals and relating observations to eruption properties (see De Angelis et al. (2019) for a review). However, they are not always applicable and may result in inaccurate infrasound-derived estimates of eruption parameters (e.g., Caplan-Auerbach et al., 2010; Johnson & Miller, 2014), which can negatively impact hazard assessment and monitoring efforts. In order to improve infrasound-derived constraints of eruption properties and leverage infrasound observations to learn more about eruptive processes and jet dynamics, we need to revisit these assumptions and consider more realistic source models (Matoza et al., 2009, 2013).

1.1 Infrasound Radiation Pattern

Many volcano infrasound studies describe the acoustic source as a point monopole source in a homogeneous half-space, which has an isotropic (equal in all directions) radiation pattern (e.g., Vergniolle & Brandeis, 1996; Johnson & Miller, 2014; Yamada et al., 2017; De Angelis et al., 2019). It is challenging to measure the radiation pattern for a volcanic eruption because most infrasound sensors are deployed on Earth's surface. Several studies have utilized surrounding topography to improve the vertical coverage of infrasound sensors (Johnson et al., 2008; Rowell et al., 2014; McKee et al., 2017) while recent work suspended infrasound sensors from tethered aerostats (Jolly et al., 2017; Iezzi et al., 2019) and observed anisotropic (different in different directions) radiation patterns.

There are several possible reasons why volcanic eruptions may have anisotropic radiation patterns. First, the radiation pattern may be a propagation artifact caused by the scattering of acoustic waves from complex volcanic topography (Lacanna & Ripepe, 2013; Kim & Lees, 2014; Lacanna et al., 2014; Kim et al., 2015; Fee et al., 2017; Lacanna & Ripepe, 2020). Second, while many studies assume a monopole source mechanism, others have argued for a dipole (Woulff & McGetchin, 1976; Johnson et al., 2008; Caplan-Auerbach et al., 2010) or multipole (Kim et al., 2012) source mechanism, which have anisotropic radiation patterns. Third, a spatially distributed source can appropriately be described as compact or a point source when the source dimension is small compared to the characteristic wavelength ($ka \ll 1$ where a is the source dimension and k is the wavenumber with $k = 2\pi/\lambda = 2\pi f/c$ where λ is the wavelength, f is the frequency and c is the speed of sound). For many volcanic eruptions $ka \sim 1$ and finite source effects, which are when acoustic waves from different parts of the source arrive at the receiver at different times, may result in an anistropic radiation pattern. Finally, Matoza et al. (2013) considered modern jet noise literature (e.g., Tam, 1998) and proposed that volcanic eruption sources are likely highly directional with respect to angle from the jet axis (this was the motivation for the observational studies of Rowell et al. (2014); McKee et al. (2017); Jolly et al. (2017) and Iezzi et al. (2019)). The simulations that we present here neglect topography but naturally capture finite source effects, possible dipole contributions and other fluid dynamic complexities that may be present in real eruptions.

1.2 Wave Propagation

Another common approximation in volcano infrasound studies is linear wave propagation, which is justified for sufficiently small pressure perturbations (Blackstock, 2000; Atchley, 2005; Matoza et al., 2019). In this limit, changes in sound speed from changes in temperature are negligible, and fluid particle velocities are small compared to the sound speed such that advection is also negligible. Volcanic eruptions, however, are violent phenomena that can generate large pressure amplitudes and large Mach number fluid motions, such that nonlinear propagation effects might be important (Marchetti et al., 2013; Johnson, 2018; Maher et al., 2020).

In recent work, Anderson (2018) and Maher et al. (2020) performed nonlinear acoustic simulations of acoustic waves radiating from a region of initial high density or pressure. In their simulations, the sound speed depends on the temperature but fluid flow and advection were not included. Anderson (2018) applied scaling analysis from the chemical/nuclear explosion literature to volcanic eruptions and showed how a single eruption simulation can be scaled for a range of eruption energies, which reduces computational expense. Maher et al. (2020) used a quadspectral density-based nonlinear indicator to detect and quantify wavefront steepening, which could be used to identify nonlinear propagation effects in field observations. In contrast to the work of Anderson (2018) and Maher et al. (2020), Brogi et al. (2018) performed nonlinear computational aeroacoustic simulations that include both acoustic waves and fluid flow, with the acoustic waves excited by fluid flow from a vent. They focused on short duration explosions and their simulations show an acoustic wave propagating away from the vent in all directions, trailed by a jet of eruptive fluid extending upwards from the vent. Brogi et al. (2018) showed that the radiation pattern became more anisotropic as the exit velocity was increased, with larger pressure amplitudes above the vent than to the side. Due to their use of a lattice Boltzmann numerical method, however, their simulations were limited to subsonic velocities ($M < 0.5$ where M is the Mach number).

1.3 Jet Dynamics

The fluid dynamics during a volcanic eruption can be extremely complex. Near the vent, erupted material forms a momentum-driven jet, which is often referred to as the gas thrust region. As the erupted material rises, it can expand and form a plume by entraining and heating the surrounding atmospheric air. If sufficient entrainment occurs, the plume can become buoyant and continue to rise. Otherwise, the plume can collapse and form a pyroclastic density current (Sparks & Wilson, 1976; Neri & Macedonio, 1996; Clarke et al., 2002; Neri et al., 2003; Koyaguchi & Suzuki, 2018). There has been extensive modeling of plume (Wilson et al., 1978, 1980; Bursik & Woods, 1991; Ogden, Glatzmaier, & Wohletz, 2008) and jet dynamics (Woods, 1988; Bursik, 1989; Ogden, Wohletz, et al., 2008; Koyaguchi et al., 2010; Ogden, 2011; Suzuki & Koyaguchi, 2012; Koyaguchi et al., 2018). The majority of modeling work has used steady state vent conditions and studied the development and evolution of volcanic jets and plumes. Cerminara et al. (2016) performed large-eddy simulations (LES) of steady volcanic plumes and the associated infrasound signal. While their study was predominantly focused on plume dynamics, they showed that infrasound can be generated by fluid flow at the vent as well as from turbulent eddies within the plume. Our study is complementary to the work of Cerminara et al. (2016) as we consider unsteady vent conditions and focus on the volcanic jet.

The two dominant controls on jet dynamics are exit velocity and pressure at the vent. Ogden, Wohletz, et al. (2008) and Koyaguchi et al. (2018) examined the influence of vent pressure on steady jet dynamics. For over-pressurized vents (vent pressure greater than atmospheric pressure), their simulations show underexpanded jets with complex flow structures, including standing shock waves (Mach disks and barrel shocks) and the flow partitioning into an outer sheath that moves faster than the inner core. For pressure balanced jets, there are no standing shock waves or flow partitioning but vortex rings develop on either side of the jet. Suzuki and Koyaguchi (2012) examined the impact of exit velocity on jet dynamics for steady state vent conditions and suggest that the efficiency of entrainment decreases with increasing exit velocity, which hampers the development of the jet into a buoyant plume and can lead to collapse. Other factors that might impact jet dynamics are vent radius and geometry (Koyaguchi et al., 2010; Ogden, 2011) and the contrast in fluid properties between the eruptive fluid and the atmosphere, but for simplicity we do not examine these effects in our study.

Several studies have used shock-tubes to study volcanic eruptions and their infrasound signals in the laboratory. Medici et al. (2014) used a high-speed camera to track shockwaves generated by a pressure gun and scaled their results to use strong shock theory to estimate explosive energy released by eruptions at Sakurajima. Swanson et al. (2018) examined the sensitivity of jet noise to vent geometry and demonstrated that, in addition to acoustic sources within the jet, vent and conduit processes are likely to be significant sources of volcanic infrasound. Peña Fernández et al. (2020) performed laboratory measurements of a shock tube in an anechoic chamber and studied the acoustic signal of a starting supersonic jet. Our simulations of the start-up of a supersonic jet are complementary to this study, although our jet was pressure-balanced with the atmosphere rather than over-pressurized. Peña Fernández et al. (2020) were able to identify the different sources of supersonic jet noise and map the sources in the time and frequency domains, which will help to identify supersonic jet noise in future field observations.

It can be challenging to directly measure exit velocities as the near-vent environment is extremely hazardous and frequently obscured by volcanic gases. Due to the unique nature of Stromboli (Italy) and Yasur (Vanuatu), Taddeucci et al. (2012, 2014, 2015) and Gaudin et al. (2014) were able to use high-speed cameras to track erupted pyroclasts and pressure waves, and observed velocities of up to 405 m/s. Other studies have used indirect observations to infer exit velocities. Marchetti et al. (2013) used a thermal camera while Yokoo and Ishihara (2007) and Ishihara (1985) relied upon visual observations of luminance changes to track shock condensation and observed propagation at supersonic velocities. Caplan-Auerbach et al. (2010) and Perttu et al. (2020) inverted infrasound observations for exit velocity for plume-forming eruptions and obtained values ranging from 43 to 220 m/s (although this approach involves several modeling assumptions). Wilson (1976) and Wilson et al. (1980) combined geological observations and physical modeling to estimate exit velocities with values as high as 600 m/s (Bercovici & Michaut, 2010; Yarushina et al., 2015). In this study, we examine the influence of the exit velocity on the observed infrasound signal and consider velocities ranging from subsonic to supersonic.

1.4 Overview

Despite substantial work on volcano infrasound and jet dynamics, there are very few modeling studies linking jet dynamics with infrasound observations (e.g., Cerminara et al., 2016; Brogi et al., 2018). This is because it is computationally challenging to simulate acoustic waves along with fluid flow. Most computational fluid dynamics methods introduce artificial dissipation to handle shocks at the expense of overdamping acoustic waves (Lele, 1997).

Here, we build upon the existing jet dynamics (e.g., Ogden, Wohletz, et al., 2008; Suzuki & Koyaguchi, 2012; Koyaguchi et al., 2018) and volcano infrasound (e.g., Anderson, 2018; Maher et al., 2020) literature by performing two-dimensional (2D) simulations of idealized unsteady volcanic eruptions and their associated infrasound radiation. Simulations are performed using the nonlinear computational aeroacoustics code, CharLES^X (Khalighi et al., 2011; Ma et al., 2018), which is a LES code that can simulate fluid flow and acoustic waves at the same time. We consider simplified eruptions of pressure-balanced jets (vent pressure equal to atmospheric pressure) where the eruptive fluid has the same composition as the atmospheric air. Our modeling approach is similar to Cerminara et al. (2016) although they considered more realistic compositions of erupted material whereas we model pure-air eruptions. Our results are complementary as Cerminara et al. (2016) focused on steady-state eruptions and plume dynamics whereas we focus on unsteady eruptions and the volcanic jet. The simulations presented here also extend the results of Brogi et al. (2018) by considering higher exit velocities (sonic and supersonic).

The manuscript is organized as follows. In Section 2, we discuss acoustics and present the analytical solution for a monopole line source that we compare with our simulation results. In Section 3, we present the nonlinear computational aeroacoustics code, CharLES^X. In Section 4, we show our simulation results for a range of exit velocities, invert the infrasound signal for erupted volume, and examine the simulated radiation pattern. In Section 5, we discuss our results in the context of nonlinear propagation, finite source effects, jet dynamics, as well as presenting some opportunities for future work. We then conclude in Section 6.

2 Acoustics

A common approximation in volcano infrasound studies is to describe the acoustic source as a point monopole in a homogeneous half-space and assume linear wave propagation (e.g., Vergniolle & Brandeis, 1996; Johnson & Miller, 2014; Yamada et al., 2017; De Angelis et al., 2019). For a monopole point source radiating in a 3D whole space, the pressure perturbation is given by (Lighthill, 1952)

$$\Delta p(R,t) = \frac{\rho_0}{4\pi R}\ddot{V}(t - R/c_0), \tag{1}$$

where Δp is the pressure perturbation, V is the volume and ρ_0 is the density of displaced atmospheric air, R is the distance from the source to receiver, c_0 is the background speed of sound, and t is time. In many volcano infrasound studies the volume of displaced atmospheric air, V, is assumed to be equal to the volume of erupted material (e.g., Fee et al., 2017).

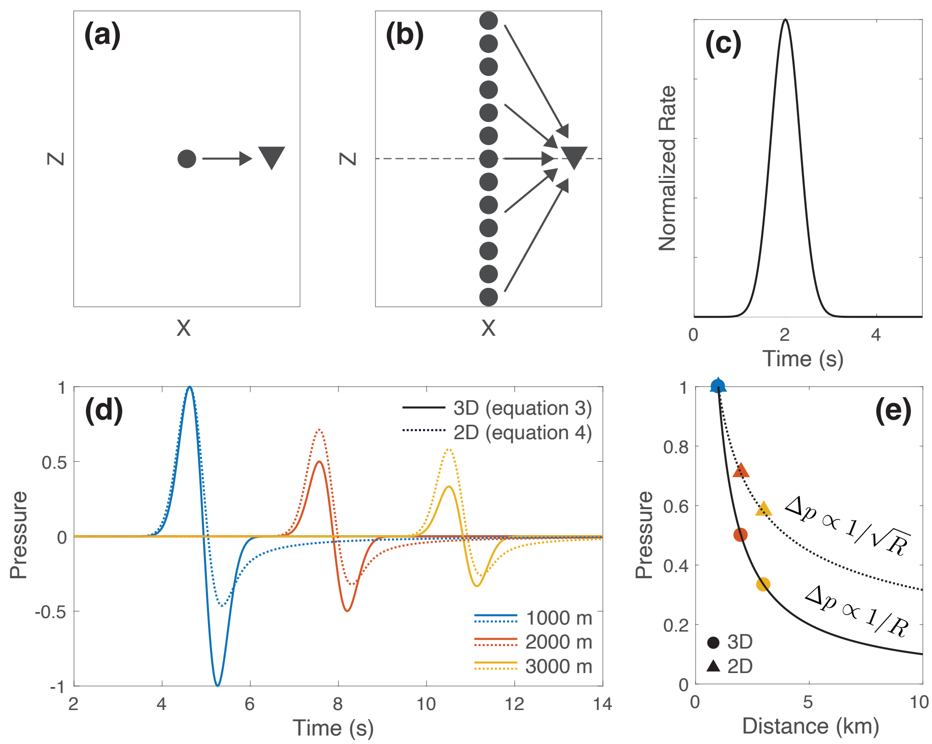

Figure 1. (a) Map-view schematic of a point source in 3D. The source is denoted by the circle and the receiver by the triangle while the arrow indicates the propagation of acoustic waves. X and Z are the two horizontal dimensions. (b) Schematic of a line source in 3D, which is invariant in the Z direction. Dashed line indicates the location of the 2D slice through the 3D domain. (c) Normalized rate, which is the source function that excites acoustic waves. In 3D, this is volume rate, $\dot{V}$ (m^3/s), whereas in 2D this is area rate, $\dot{A}$ (m^2/s). (d) Analytical infrasound signals at 1000 m (blue), 2000 m (red), and 3000 m (yellow) from the point source (solid) and line source (dotted) computed using equations 2 and 3, respectively, and the rate shown in (c). (e) Peak pressure as a function of distance for point (circle) and line (triangle) sources. Black lines show $1/R$ (solid) and $1/\sqrt{R}$ (dotted) decay. The infrasound signals are normalized by the peak amplitude at 1000 m.

In order to take into account the bounding effect of Earth's surface, equation 1 can be modified for radiation into a half space (Johnson et al., 2012; Johnson & Miller, 2014; Yamada et al., 2017; Watson et al., 2019):

$$\Delta p(R,t) = \frac{\rho_0}{2\pi R}\ddot{V}(t - R/c_0), \tag{2}$$

where the radiation angle is reduced from 4π to 2π. Equations 1 and 2 have an isotropic radiation pattern (same in all directions). Example infrasound signals generated by a monopole point source with a Gaussian volume rate in a half space are shown in Figure 1.

In this study, we perform computational aeroacoustic simulations in 2D Cartesian coordinates for computational efficiency. Our 2D model assumes invariance in one horizontal coordinate direction, which changes the monopole point source to a line source oriented normal to the propagation plane. In order to compare between our computational simulations and analytical models, we consider the monopole line source solution (analogous to the 3D monopole point source solution of equation 2):

$$\Delta p(R,t) = \frac{\rho_0}{2\pi}\int_0^{t-R/c_0} \frac{\ddot{A}(\tau)}{\sqrt{(t-\tau)^2 - R^2/c_0^2}}\, d\tau, \tag{3}$$

where A is the area of displaced atmospheric air.

Acoustic waves excited by a line source behave differently to those excited by a point source (Lighthill, 1952; Lacanna & Ripepe, 2013; De Groot-Hedlin, 2016). For a point source, acoustic waves propagate directly from the source to receiver (Figure 1a). For a line source, acoustic waves from different places along the line source have different source-receiver distances and hence arrive at different times (Figure 1b). Waves originating from further away along the line source arrive later and, due to the interference of waves from different source locations, the signal observed at the receiver is characterized by a lower amplitude rarefaction with longer duration (Figure 1d). For a point source, the amplitude decays as $1/R$ whereas for a line source the amplitude decays as $1/\sqrt{R}$ (Figure 1e).

3 Computational Aeroacoustics and CharLES^X

In this section we describe the computational aeroacoustics code, CharLES^X, that we use to perform our nonlinear simulations. CharLES^X is an aeroacoustics code that can simulate both fluid flow and acoustic waves, where the acoustic waves are generated naturally in the simulations by the compressible fluid dynamics. This differs from previous nonlinear infrasound studies by De Groot-Hedlin (2012), Anderson (2018), and Maher et al. (2020) that used acoustic solvers with acoustic waves excited by a zone of initial high pressure or density (an equivalent acoustic source) and did not directly model the complex fluid dynamics in the source region. Gravity is neglected due to our focus on jet dynamics rather than the plume.

CharLES^X is an unstructured mesh, finite-volume, LES code that is widely used in studies of jet noise and other aeroacoustics applications (Khalighi et al., 2011; Nichols et al., 2012; Hickey & Ihme, 2014; Brès et al., 2016; Ma et al., 2018; Chung et al., 2019; Jaravel et al., 2019; Lyrintzis & Coderoni, 2019; Ma et al., 2019). The code solves the filtered compressible Navier-Stokes equations in fully conservative form:

$$\partial_t \bar{\rho} + \nabla \cdot (\bar{\rho}\tilde{\boldsymbol{u}}) = 0, \tag{4a}$$

$$\partial_t (\bar{\rho}\tilde{\boldsymbol{u}}) + \nabla \cdot (\bar{\rho}\tilde{\boldsymbol{u}}\tilde{\boldsymbol{u}}) = -\nabla \bar{p} + \nabla \cdot \bar{\boldsymbol{\tau}}_{\nu+t}, \tag{4b}$$

$$\partial_t (\bar{\rho}\tilde{e}_t) + \nabla \cdot (\bar{\rho}\tilde{\boldsymbol{u}}\tilde{e}_t) = -\nabla \cdot (\bar{p}\tilde{\boldsymbol{u}}) + \nabla \cdot (\bar{\boldsymbol{\tau}}_{\nu+t} \cdot \tilde{\boldsymbol{u}}) - \nabla \cdot \bar{\boldsymbol{q}}_{\nu+t}, \tag{4c}$$

where tilde and over-bar notations denote Favre and Reynolds filtering, respectively, which arise in the formal derivation of the LES equations for compressible flows (see Garnier et al. (2009) for details). Here, ρ is the density, $\boldsymbol{u}$ is the velocity vector, p is the pressure, $\boldsymbol{\tau}_{\nu+t} = (\mu_\nu + \mu_t)\left(\nabla\tilde{\boldsymbol{u}} + (\nabla\tilde{\boldsymbol{u}})^T - \frac{2}{3}(\nabla \cdot \tilde{\boldsymbol{u}})\boldsymbol{I}\right)$ is the viscous stress tensor, $\boldsymbol{I}$ is the identity matrix, $e_t = e_s + \frac{1}{2}\tilde{\boldsymbol{u}} \cdot \tilde{\boldsymbol{u}}$ is the specific total energy, $\boldsymbol{q}_{\nu+t} = -(\lambda_\nu + \lambda_t)\nabla T$ is the heat flux vector, and T is the temperature. Subscripts ν and t denote viscous and turbulent contributions, respectively. Sensible specific energy e_s, as well as molecular dynamic viscosity μ_ν and thermal conductivity λ_ν are obtained using the Cantera library (Goodwin et al., 2018) for thermodynamic, chemical kinetic, and transport processes although in this work we neglect any reactive chemistry effects.

Equations 4 are time-advanced using a third-order explicit Runge-Kutta time-stepping scheme (Hickey & Ihme, 2014; Ma et al., 2018). Spatial discretization is performed using a hybrid spatial differencing approach that switches between a low-dissipation centered (fourth-order accurate on uniform meshes) and a lower-order (either first-order or second-order essentially non-oscillatory, or ENO) scheme (Khalighi et al., 2011; Hickey & Ihme, 2014). The lower-order schemes are activated only in regions of high local density variation (e.g., shocks) using a threshold-based sensor (Hickey & Ihme, 2014). Boundary conditions are enforced using a penalty method in terms of characteristic variables (Poinsot & Lelef, 1992). When solving the Navier-Stokes equations, it is critical to account for the effects of the unresolved turbulence on the resolved flow using a sub-grid model (Khalighi et al., 2011). Sub-grid stresses are modeled using the Vreman (2004) eddy-viscosity model and a constant turbulent Prandtl number of 0.5.

The maximum resolvable frequency is controlled by the time step, Δt, and the spatial resolution, Δx, which are linked through the Courant Friedrichs Lewy (CFL) criterion of CFL=1 (Courant et al., 1967). Given the fourth-order central spatial scheme and the third-order Runge-Kutta time-stepping scheme, the maximum resolvable frequency is given by (Tam & Webb, 1993)

$$f_{\max} \approx \frac{0.4c}{2\Delta x}, \tag{5}$$

and the minimum resolvable frequency is given by

$$f_{\min} \approx \frac{0.4c}{2L}, \tag{6}$$

where L is the spatial extent of the domain and c is the sound speed.

As previously mentioned, CharLES^X is a LES code, which means that length scales smaller than the grid resolution are modeled using a sub-grid model (Vreman, 2004). An alternative to LES is Direct-Numerical Simulation (DNS), which requires that the grid resolution is sufficient to capture length scales down to the Kolmogorov scale. The Kolmogorov length scale, η, in the vicinity of the vent can be estimated by (Pope, 2001)

$$\eta \approx D\mathrm{Re}^{-3/4}, \tag{7}$$

where D is the diameter of the vent and Re is the Reynolds number, which is given by

$$\mathrm{Re} = \frac{\rho U D}{\mu}, \tag{8}$$

where U is the exit velocity and μ is the dynamic viscosity of air (approximately $1{\times}10^{-5}$ Pa s).

In this study, we consider a vent diameter of 60 m and exit velocities up to 588 m/s. The vent Reynolds number is therefore $\mathrm{Re} \approx 1{\times}10^9$ and the Kolmogorov length scale is $\eta \approx 1{\times}10^{-5}$ m. Attempting to resolve these length scales even for just one vent diameter downstream would yield a 2D mesh size the order of $1{\times}10^{12}$ elements with a time step of $\Delta t \approx 1 \times 10^{-7}$ s, which is prohibitively computationally expensive. In addition, the high resolution provided by DNS is superfluous for volcano acoustic purposes. For the simulations considered here, the acoustic disturbances generated by the smallest eddies have a frequency of $f_\eta = \mathrm{Re}^{1/2}U/L \approx 1 \times 10^6$ Hz and are attenuated due to viscosity on a length scale of approximately 1 m. Hence, there is no need to resolve down to these short length scales (high frequencies).

LES combined with a low-dissipation numerical scheme allows the fluid dynamical effects of the smallest scales to be modeled via a sub-grid scale model while preserving the large scale motion, so long as the length scales of interest are significantly greater (frequencies of interest are significantly lower) than those generated by the smallest fluid length scales, as is the case for volcano acoustics. Therefore, LES is a practical and computationally tractable alternative to DNS and provides the resolution required by the volcano acoustics community.

CharLES^X can handle multiple, interacting fluids, which may be important to consider because the eruptive fluid generally has a different composition than the surrounding atmosphere. In this work, however, the erupted fluid has the same composition as the atmosphere, which allows us to focus on the influence of exit velocity. CharLES^X can also handle particle-laden flows (Mohaddes et al., 2021), with particles obeying their own Lagrangian equations of motion and having velocities that might differ from that of the gas. While this more rigorous treatment of ash particles has been shown to have important effects in conduit flow and jets (Dufek & Bergantz, 2007; Dufek et al., 2012; Matoza et al., 2013; Benage et al., 2016; Cerminara et al., 2016), we defer these effects for future work.

4 Results

Here, we perform 2D computational aeroacoustic simulations of idealized pure-air impulsive volcanic eruptions using CharLES^X. We focus on short-duration strombolian and vulcanian eruption styles because they occur frequently and there is a wealth of available data that can be used to inform and validate modeling efforts (e.g., Matoza et al., 2014). These smaller eruptions are computationally simpler and more tractable to simulate yet exhibit many of the complex processes influencing infrasound generation and propagation (e.g., entrainment, shocks), with findings transferable to more hazardous sub-plinian/plinian eruptions. Our simulation results are compared with the compact monopole model and finite-difference linear acoustics simulations (hereafter referred to as linear simulations; Almquist & Dunham, 2020) to investigate and quantify deviations from linear acoustics and finite source effects.

4.1 Simulation Setup

The 2D computational domain is shown in Figure 2 and is invariant in the horizontal z direction (i.e., we simulate an infinite planar jet). The domain is discretized into rectangular elements with 2 m resolution at the vent and stretched horizontally to 10 m at the boundaries. The maximum resolvable frequency is 35 Hz near the vent and 7 Hz at the boundaries (equation 5) while the minimum resolvable frequency is 0.2 Hz (equation 6). The domain is initialized with stationary air with a composition of 23% oxygen and 77% nitrogen, which defines the specific gas constant and specific heat (Goodwin et al., 2018). The pressure is 101,325 Pa and the temperature is 300 K, which gives a speed of sound of 347 m/s.

The computational domain is bounded at the bottom by Earth's surface with a 60 m diameter vent in the center and by outflow boundaries on the other three sides. At the outflow boundaries, a constant pressure condition is applied ($p_{\text{out}} = 101,325$ Pa). This simple boundary condition causes small reflections when acoustic waves interact with the boundary. However, the boundaries are sufficiently far away that the simulations finish before the small reflections interact with the area of interest. Earth's surface is mod-

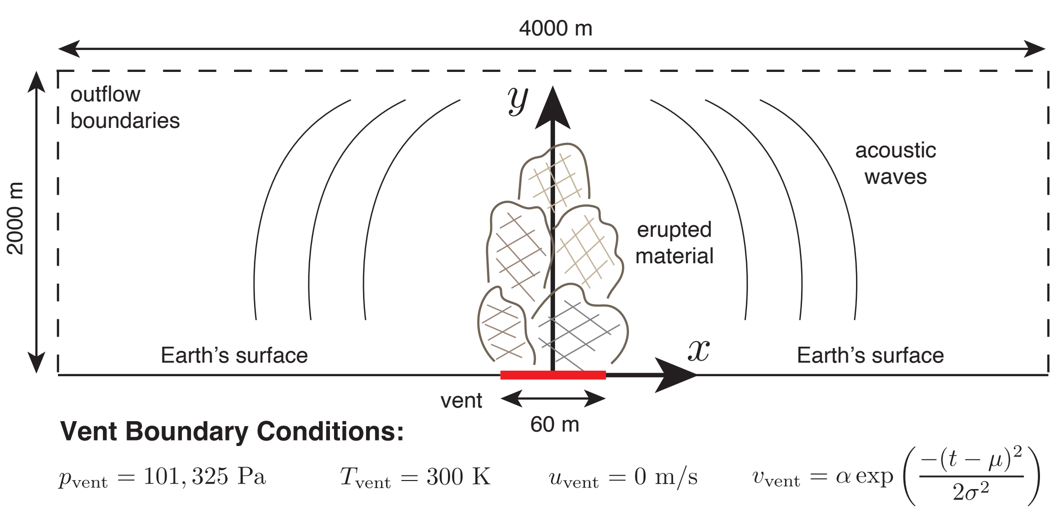

Figure 2. Schematic of two-dimensional computational domain. The bottom of the domain is divided into Earth's surface and the vent (red) where material is erupted. The four boundary conditions applied at the vent are shown below the schematic.

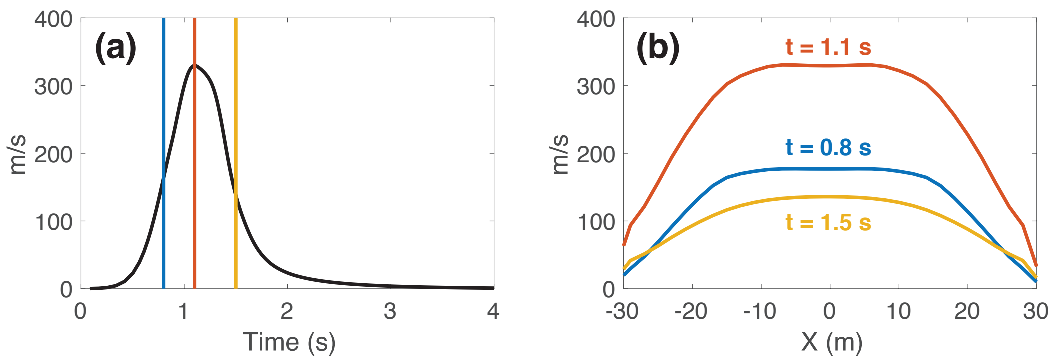

Figure 3. (a) Time series of vertical velocity at the center of the vent. (b) Vertical velocity spatial profile across the vent at (blue) $t = 0.8$ s, (red) $t = 1.1$ s, and (yellow) $t = 1.5$ s. The vertical lines in (a) correspond to the times of the velocity profiles shown in (b).

eled as an adiabatic wall boundary. At the vent, the two components of velocity, pressure, and temperature are specified. The horizontal velocity, u, is set equal to zero while the pressure and temperature are prescribed to be the same as the atmospheric conditions (101,325 Pa and 300 K, respectively). The vertical velocity, v, is prescribed as a

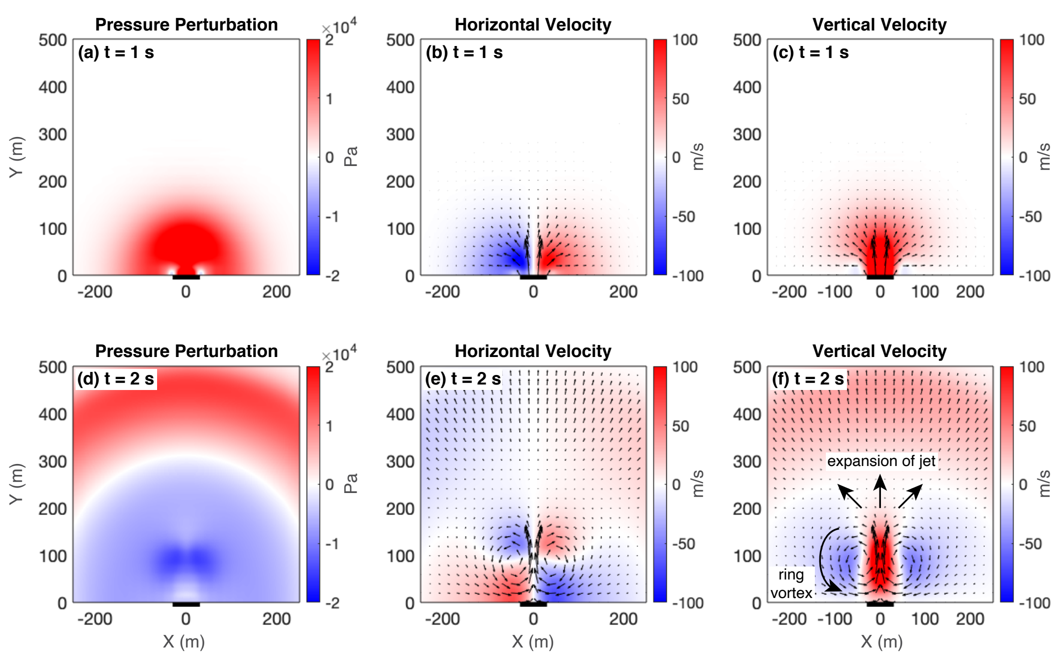

Figure 4. Snapshots of (a and d) pressure perturbation, (b and e) horizontal velocity, and (c and f) vertical velocity at (top) 1 s and (bottom) 2 s. The maximum exit velocity is 330 m/s and the vent location is indicated by the thick black line at the base of the plots. Velocity vectors are annotated on the horizontal and vertical velocity plots and show the development of vortex rings (Shariff & Leonard, 1992) on either side of the vent, as annotated in (f).

Gaussian pulse:

$$v(t) = \alpha \exp\left(\frac{-(t-\mu)^2}{2\sigma^2}\right), \tag{9}$$

where α is the maximum amplitude, μ controls the center of the pulse and σ determines the width. In this study we use $\mu = 1$ s, and $\sigma = 0.25$ s (an example vertical velocity time series is shown in Figure 3a). The vertical velocity varies spatially across the vent with a flat maximum in the center and tapering to zero at the edges of the vent, based on the experimental work of Swanson et al. (2018) (example vertical velocity spatial profiles are shown in Figure 3b). The value of σ is chosen to approximate the volumetric flow rates observed at Sakurajima Volcano by Fee et al. (2017).

For the Navier-Stokes equations, unlike the Euler equations, there is no difference in the number of boundary conditions specified for subsonic and supersonic inflows (Nordström & Svärd, 2005; Svärd et al., 2007). The boundary conditions are weakly enforced and therefore there can be some differences between the prescribed boundary condition and the simulation value. Time series of vertical velocity at the vent can have lower amplitude and more extended decay that the prescribed Gaussian function and the pressure at the vent can deviate from atmospheric pressure. We define $v_{\max}$ as the maximum value of vertical velocity at the vent and note that due to the weak enforcement of the boundary conditions $v_{\max} < \alpha$. Due to the very small viscosity values, the no-slip condition on Earth's surface is effectively not enforced, as would be appropriate in the limit of the inviscid Euler equations.

4.2 Simulation Results

In this section, we present a detailed analysis of a single simulation for $v_{\max} = 330$ m/s ($M = 0.95$). The vertical velocity at the center of the vent ($x = 0$) is shown in Figure 3a and several snapshots of the velocity profile across the vent are shown in Figure 3b.

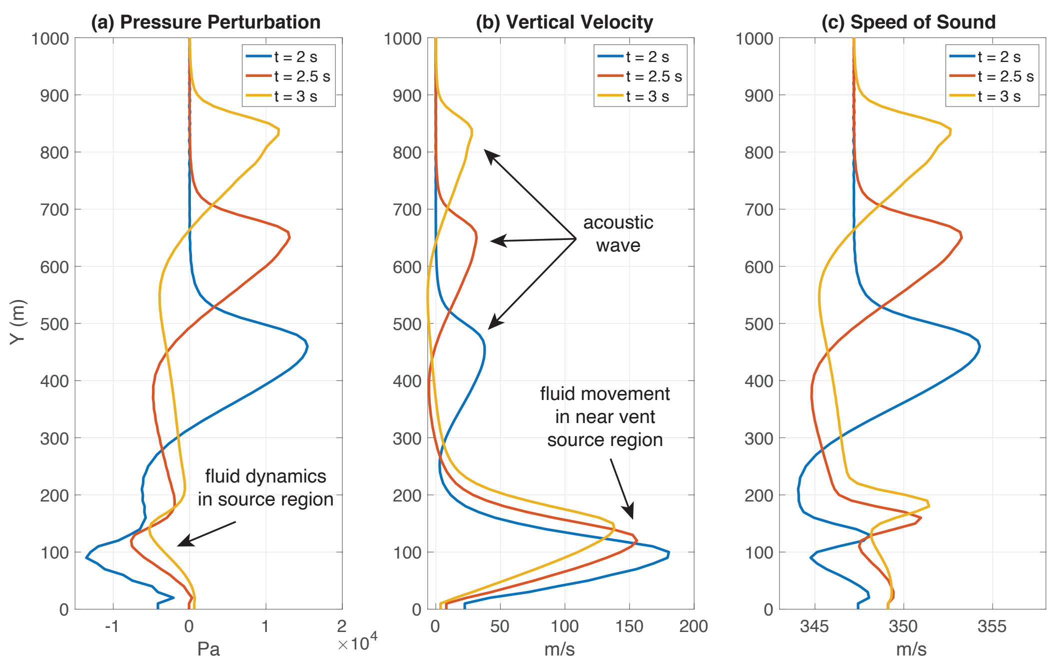

Figure 5. Vertical profiles of (a) pressure perturbation, (b) vertical velocity, and (c) speed of sound for a line of receivers above the vent ($x = 0$ m). Profiles are shown for three times: (blue) $t = 2$ s, (red) $t = 2.5$ s, and (yellow) $t = 3$ s.

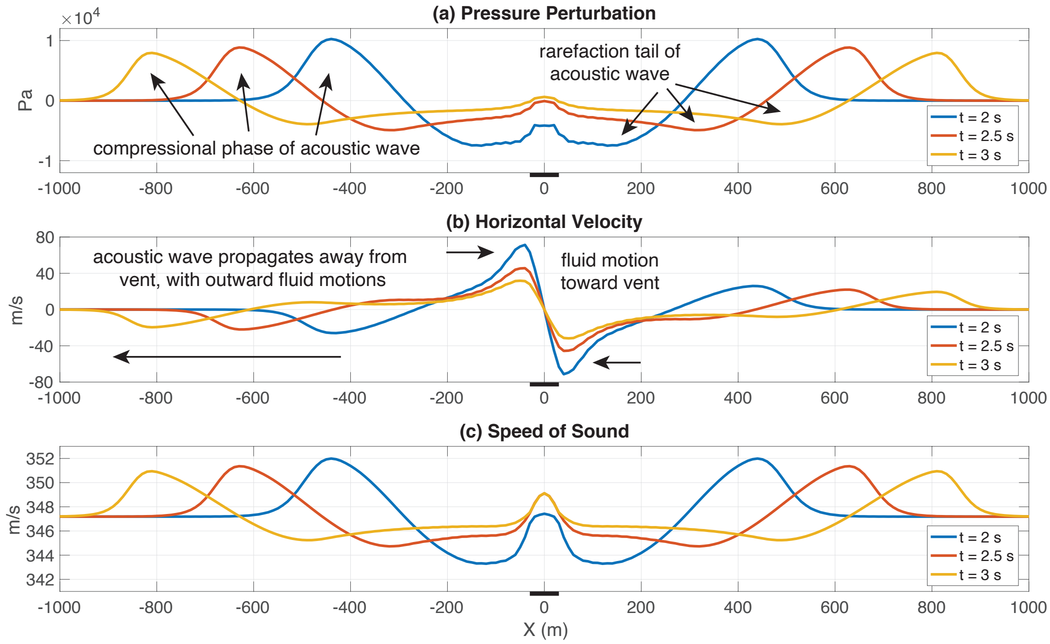

Figure 6. Horizontal profiles of (a) pressure perturbation, (b) horizontal velocity, and (c) speed of sound for a line of receivers along the base of the domain ($y = 0$ m). Profiles are shown for three times; (blue) $t = 2$ s, (red) $t = 2.5$ s, and (yellow) $t = 3$ s. The vent location is indicated by the black line at the base of the plots.

Snapshots of the pressure perturbation, horizontal and vertical velocity near the vent are shown in Figure 4. Figure 5 shows vertical profiles above the vent of pressure perturbation, vertical velocity, and speed of sound. Figure 6 shows horizontal profiles along the base of the domain of pressure perturbation, horizontal velocity, and speed of sound.

During the eruption, fluid is erupted out of the vent. This pushes on the atmosphere and generates an initial compressional pulse of pressure that propagates radially outwards from the vent. This is part of the acoustic pulse that is routinely observed in infrasound studies. As the pulse propagates further from the vent, a rarefaction tail, which is a well-known feature of 2D acoustics, develops (Figures 5a and 6a). The rarefaction is not clearly visible in the early time snapshots shown in Figure 4 because the acoustic pulse has not sufficiently separated from the fluid dynamics near the vent. In addition to the pressure pulse, the acoustic wave also causes particle motions radially away from the vent.

A jet of erupted material develops behind the acoustic wave as the eruption continues (Figure 4). The jet exhibits complex fluid dynamics and, for the pressure balanced vent conditions considered here, has a negative pressure perturbation. Directly above the vent, fluid rapidly moves vertically upwards. At the top part of the jet, the erupted fluid pushes outwards, forcing the atmospheric air into outward motion and causing the jet to expand with fluid moving horizontally away from the vent and vertically upwards. Outside of the vent, the fluid moves slowly downwards and fluid is recirculated horizontally back towards the vent at the base of the jet. This causes the formation of vortex rings (Shariff & Leonard, 1992) on either side of the vent (Figure 4e and 4f).

The acoustic waves steepen and the rarefaction tail becomes longer with time as the waves propagate farther from the vent (Figures 5a and 6a). Compression of the atmospheric air causes appreciable increases in temperature and consequently the local speed of sound. This causes the high pressure parts of the waveform to propagate faster, causing wavefront steepening and elongating the rarefaction tails (Hamilton & Blackstock, 2008). Anderson (2018) and Maher et al. (2020) have suggested this phenomena as the cause of asymmetric waveforms recorded during volcano infrasound studies. For our simulations, however, the speed of sound changes shown in Figures 5c and 6c are relatively small ($\sim 2\%$) suggesting that this is not the relevant nonlinearity. Instead, we contend that the nonlinear behavior is likely due to the nonlinear advection terms in the Navier-Stokes equations becoming significant as the fluid velocity approaches the speed of sound. More details about this are included in the Discussion section.

4.3 Exit Velocity

In this section, we examine the sensitivity of the infrasound signal to the exit velocity. We first examine the forward problem of calculating the infrasound signal from the eruptive rate and compare results of our nonlinear simulations to the linear acoustic monopole source model (equation 3). We then consider the inverse problem of inverting infrasound observations for the erupted volume rate and compare the inversion result with the true solution from our simulations.

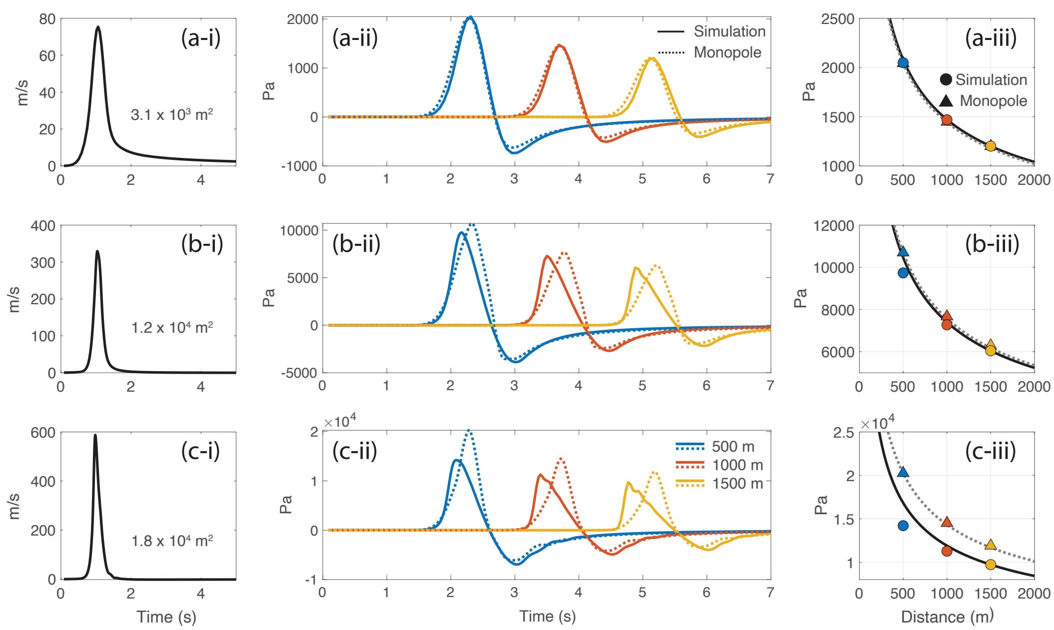

Figure 7. Comparison of infrasound signals from simulations (solid) and compact monopole model (dotted; equation 3) for eruption sources with three different exit velocities: (a) $v_{\max}$ =76 m/s ($M = 0.22$), (b) $v_{\max}$ =330 m/s ($M = 0.95$), and (c) $v_{\max}$ =588 m/s ($M = 1.69$). (i) Vertical velocity at center of vent. Numbers indicate the total erupted area. (ii) Infrasound time series recorded by probes at the base of the domain at three different distances from the center of the vent: (blue) 500 m, (red) 1000 m, and (yellow) 1500 m. (iii) Maximum pressure perturbation from the infrasound time series plotted as a function of distance for the simulations (circles) and the monopole model (triangles). The lines indicate the $1/\sqrt{r}$ decay of amplitude expected for linear propagation. The solid line is fitted to the peak amplitude of the nonlinear simulations at 1500 m distance from the vent while the dotted line is fitted to the peak amplitude of the linear acoustics model at 1500 m from the vent.

4.3.1 Forward Problem

We perform simulations for a range of exit velocities between $v_{\max} = 76$ m/s and $v_{\max} = 588$ m/s and examine the infrasound signal recorded by probes along the Earth's surface. The simulations are compared with the compact monopole model (equation 3) where the area of the displaced atmospheric air is assumed to be equal to the area of erupted material (i.e., no entrainment).

A subset of the simulation results are shown in Figure 7. For low exit velocities ($v_{\max}$ =76 m/s; Figure 7a), the simulations and monopole model are in good agreement with similar arrival times, waveform shape, and peak amplitudes. The simulated infrasound signal decays in amplitude as $1/\sqrt{r}$, as expected from linear wave propagation theory, and the waveform does not change with distance from the vent. However, for high exit velocities ($v_{\max}$ >330 m/s; Figure 7b,c), the simulations diverge from the monopole model. The simulations have lower amplitude, faster onset, and slower amplitude decay than the monopole model. The simulated infrasound signals arrive sooner than for the monopole model, which suggests that advection may be important (advection is where the acoustic wave propagates at speed of sound plus the fluid velocity in the propagation direction). In addition, the waveform changes with distance from the vent (waveform evolution with distance could be used to discriminate between nonlinear propagation versus source effects). Maher et al. (2020) performed nonlinear acoustic simulations and showed that wavefront steepening can cause an upward spectral energy transfer of up to 1% of the source level, hence some of the reduction of peak amplitude may be due to the finite frequency range of our simulations. However, as we resolve frequencies up to 35 Hz at the vent and 7 Hz at the boundaries, we expect this effect to be minimal. Figure 8b shows the normalized spectral amplitude for a subset of simulations. The majority of energy is concentrated below 1 Hz with the higher exit velocity simulations having more energy at higher frequencies ($\approx$ $2-8$ Hz), as predicted by Maher et al. (2020). The waveforms lack power above 10 Hz, and therefore are more than adequately resolved by our simulations.

Figure 8c and 8d show the peak pressure and maximum rate of change of pressure (Gee et al., 2007) as a function of exit velocity for the simulations and monopole model. This figure shows that the two solutions are in good agreement for low exit velocities but diverge as the exit velocity approaches and exceeds the speed of sound.

The simulation results presented here suggest that the compact monopole model, which assumes linear wave propagation, is an appropriate description for eruptions with low exit velocities. For high exit velocities, however, the monopole model is inappropriate and will result in an overestimation of the peak amplitude of the infrasound signal. We examine the sensitivity of the radiation pattern to exit velocity in Section 4.4 and discuss reasons for the differences between the simulations and monopole model in Section 5.

4.3.2 Inverse Problem

After examining the forward problem of calculating the infrasound signal for a given exit velocity, we now consider the inverse problem of estimating the erupted area from a given infrasound signal. We first simulate the infrasound signal for a range of exit velocities. We then invert the simulated infrasound signal at a single station on Earth's surface at 1000 m from the vent for the area rate, assuming a compact monopole source and linear wave propagation (equation 3). We assume that the area of displaced air is equal to the erupted area (i.e., no entrainment). The inverted area rate is compared with the true area rate, which is prescribed in the computational simulations. The goal of this section is to quantify how neglecting finite source effects and nonlinearities can bias estimates of the erupted volume (erupted area for our 2D simulations). Maher et al. (2019) performed a similar study using a nonlinear acoustic code and argued that waveform dis-

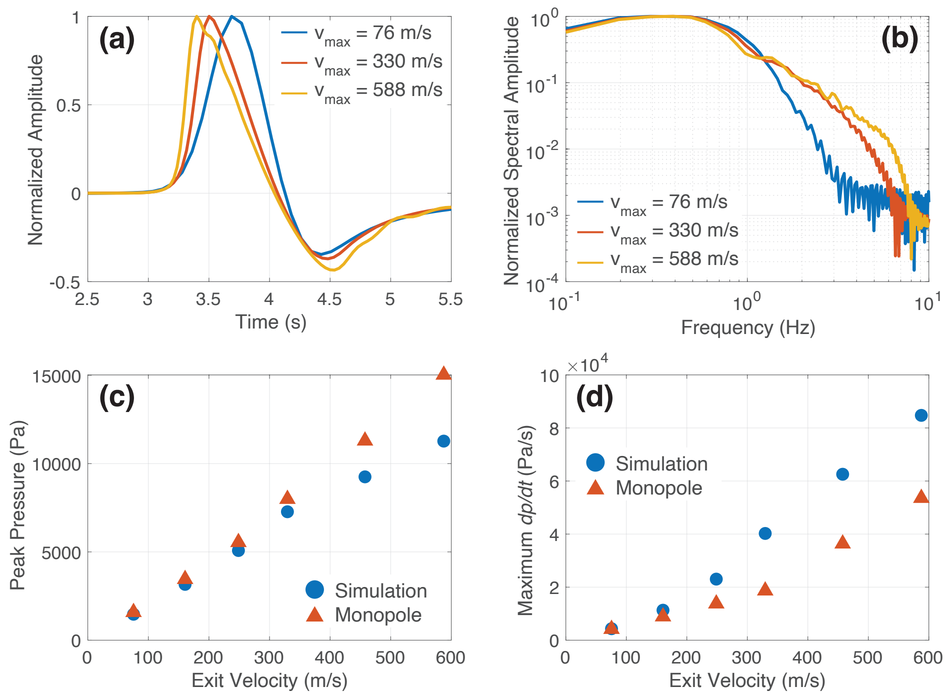

Figure 8. Normalized infrasound signal in the (a) time and (b) frequency domain for three different exit velocities; (blue) $v_{\max} = 76$ m/s, (red) $v_{\max} = 330$ m/s, and (yellow) $v_{\max} = 588$ m/s. As the exit velocity increases, the (a) wavefronts become steeper and (b) energy is transferred to higher frequencies. (c) Peak pressure and (d) maximum rate of change of pressure, dp/dt (e.g., Gee et al., 2007), of the infrasound signals from simulations (blue, circles) and the monopole model (red, triangles) as a function of maximum exit velocity. The simulations and the monopole model are in agreement for low exit velocities. However, when the exit velocity increases, the two solutions diverge with the simulations having a lower peak pressure and higher dp/dt. Infrasound signals are recorded along Earth's surface at 1000 m from the vent.

tortions from nonlinear effects do not significantly affect volume estimates made with the linear assumption. In this work, we build upon this previous study and use the nonlinear aeroacoustics code CharLES^X, which accounts for jet dynamics and nonlinear effects in near-vent as well as nonlinear propagation, and consider a wider range of eruption amplitudes.

Equation 3 shows that the pressure perturbation in linear acoustics can be expressed as a convolution between the second time derivative of the area of displaced atmosphere, $\ddot{A}$, and a transfer function that describes the propagation, G:

$$\Delta p(r,t) = \ddot{A}(t) * G(r,t), \tag{10}$$

where $*$ denotes the time-domain convolution. The convolution operation in the time domain corresponds to multiplication in the frequency domain:

$$\Delta \hat{p}(r,\omega) = \hat{\ddot{A}}(\omega)\hat{G}(r,\omega), \tag{11}$$

where ω is the angular frequency and $\hat{}$ denotes the Fourier transformed variable. The inversion problem can then be formulated as a time-domain deconvolution, which simplifies to division in the frequency domain:

$$\hat{\ddot{A}}(\omega) = \Delta \hat{p}(r,\omega) \;/\; \hat{G}(r,\omega). \tag{12}$$

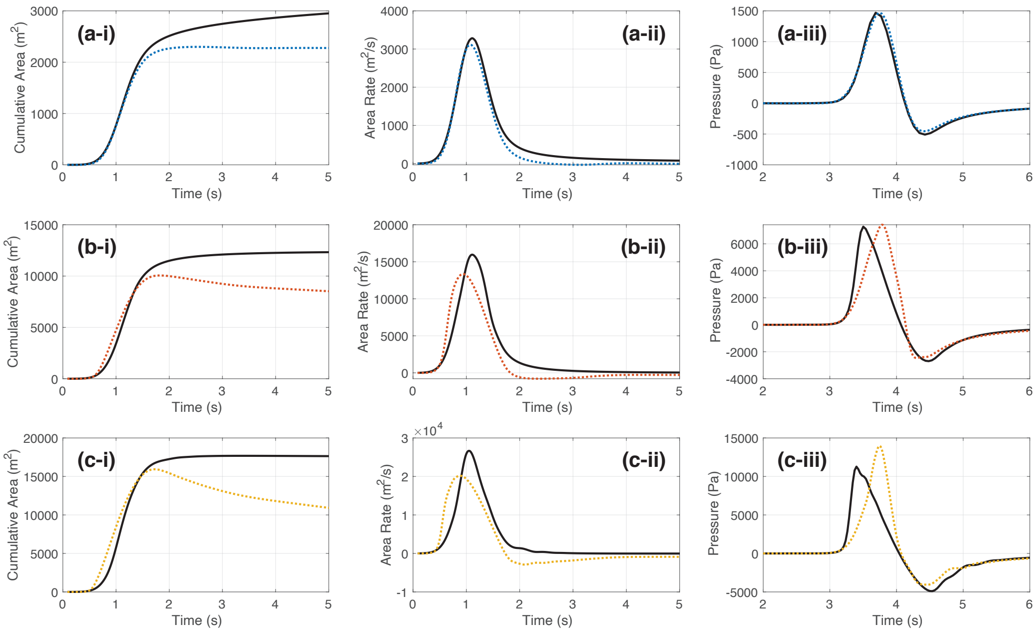

Figure 9. Comparison of true and inverted cumulative area and area rate as well as infrasound signal for three different maximum exit velocities; (a) $v_{\max}$ =76 m/s, (b) $v_{\max}$ =330 m/s, and (c) $v_{\max}$ =588 m/s. (i) Cumulative area showing true (black, solid) and inverted (colored, dotted). (ii) Area rate showing true (black, solid) and inverted (colored, dotted). The true area rate is obtained from the simulations and integrated to obtain the true cumulative area. Inverted area rate and cumulative values are calculated by inverting the simulated infrasound signal (black, solid) at a receiver 1000 m from the vent on Earth's surface (iii) assuming compact monopole model (equation 3) and integrating once or twice, respectively. (iii) Comparison of infrasound signals from simulations (black, solid) and from monopole model (colored, dashed) at 1000 m from the vent. The infrasound signal for the monopole model is calculated from the true area rate shown in (ii).

We then transform $\hat{\ddot{A}}(\omega)$ back to the time domain and integrate twice in time to obtain the area of the displaced atmospheric air, which we assume to be equal to the erupted area.

Figure 9 shows the erupted area rate and associated infrasound signal for three exit velocities. For low exit velocities ($v_{\max}$ =76 m/s; Figure 9a) the inverted area rate is in good agreement with the true value. This is expected because the simulated and monopole infrasound signals are in good agreement. However, for high exit velocities ($v_{\max}$ >330 m/s; Figure 9b and 9c), the inverted area rate diverges from the true value. The inverted area rate has a faster rise to a lower peak value and more gradual decay to a negative value of area rate. We note that future work could utilize a more sophisticated inversion scheme where the area rate is constrained to be non-negative and multiple stations are used.

The area rate can be integrated to obtain the total erupted area (Figure 9-i). For the higher exit velocities, the extended rarefaction leads to a decrease in the cumulative area. Figure 10 compares the true erupted area with the inverted erupted area at 5 s. For low exit velocities ($v_{\max} < 100$ m/s), the true and inverted areas are in good agreement. For high exit velocities, however, the inverted area underpredicts the true value. For an exit velocity of 330 m/s, the inversion procedure underpredicts the erupted area by 30%. The error increases with increasing exit velocity and for an exit velocity of 588 m/s the inversion underpredicts the erupted area by 37%.

The results presented in this section show that interpreting volcano infrasound observations with a compact monopole model, which assumes linear wave propagation, can result in substantial underestimation of the erupted rate and cumulative area, especially when the exit velocity approaches or exceeds the speed of sound. In Section 5 we explore possible reasons for the discrepancy between our simulations and the monopole model. We consider nonlinear effects during propagation (temperature dependence of sound speed and advection), entrainment and complex fluid flow in the source region, and finite source effects. We note that we have so far only considered receivers along Earth's surface. In the next subsection we explore the infrasound radiation pattern and its dependence on exit velocity.

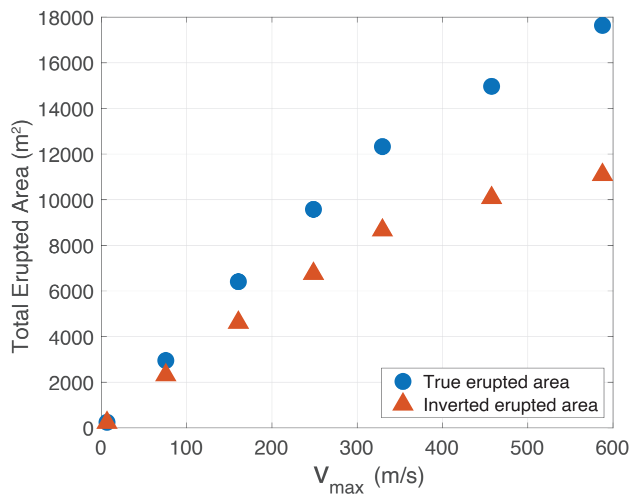

Figure 10. Total erupted area as a function of maximum exit velocity at $t = 5$ s showing (blue, circles) true and (red, triangles) inverted erupted area. The inverted erupted area is calculated by inverting the nonlinear infrasound signals recorded at 1000 m from the vent using equation 3, which assumes linear wave propagation. The inverted area agrees with the true erupted area for low exit velocities, however, for sonic and supersonic exit velocities the inverted erupted area substantially underpredicts the true erupted area.

4.4 Radiation Pattern

The compact monopole model has an isotropic radiation pattern where acoustic energy is radiated equally in all directions. In this section, we examine the radiation pattern of our simulations and compare to the monopole model. As before, we consider three different maximum exit velocities in order to investigate the dependence of the radiation pattern on exit velocity. We examine the infrasound signal at 10 probes that are located between 0° and 90° from the jet axis at 10° intervals. The probes are all 1000 m radially from the center of the vent in order to measure the acoustic radiation that would be observed by infrasound sensors in the field rather than the fluid flow close to the vent, which from Figure 4 we see is confined to within $\sim$ 200 m around the vent for the eruptions considered in this work.

For each simulation, we compute the sound pressure level and the peak pressure at each probe. The sound pressure level, measured in decibels, is commonly used in volcano infrasound and jet noise studies to describe acoustic signals (Matoza et al., 2007; Gee et al., 2008; Maher et al., 2020) and is defined as

$$\mathrm{SPL} = 20\log_{10}\left(\frac{p_{\mathrm{rms}}}{p_{\mathrm{ref}}}\right), \tag{13}$$

where p_{rms} is the root mean square pressure and p_{ref} is the reference pressure of 20 μPa.

Figure 11 shows the change in sound pressure level and peak pressure as a function of angle from the jet axis in decibels and percentage, respectively. For $v_{\max} = 76$ m/s, the radiation pattern is relatively isotropic. The sound pressure level above the vent is only 0.29 dB greater than the value measured by a probe on the Earth's surface, which corresponds to a 7% increase in intensity. Similarly, the peak pressure perturbation above the vent is 6.6% larger than on Earth's surface. For high exit velocities, the radiation pattern becomes more strongly anisotropic. For $v_{\max} = 330$ m/s, the sound pressure level is 1.9 dB greater, corresponding to an intensity increase of 53%, when measured above the vent compared to on Earth's surface. For $v_{\max} = 588$ m/s, the sound pressure level is 3.1 dB greater, corresponding to an intensity increase of 104%, when measured above the vent. Similarly, for maximum exit velocities of $v_{\max} = 330$ m/s and $v_{\max} = 588$ m/s, the peak pressure measured above the vent is 50% and 100% higher, respectively, compared to on Earth's surface. Anisotropic radiation patterns have been previously observed in the field (e.g., Jolly et al., 2017; Iezzi et al., 2019).

There are several possible reasons for the anisotropic radiation pattern. First, the compact monopole model (equation 3) is only appropriate if $ka \ll 1$. For a compact source, the source dimension is small compared to the acoustic wavelength so that waves originating anywhere within the compact source region arrive at the receiver at effectively the same time. The radiation for a compact monopole source is isotropic (equation 3 only depends on the source-receiver distance and not the receiver position). If the source dimension is large compared to the acoustic wavelength ($ka \approx 1$), then waves originating from different locations in the source region will arrive at the receiver at different times. This can result in an anisotropic radiation pattern, such as for a baffled piston (Buckingham & Garcés, 1996; Garcés, 2000; Watson et al., 2019) where the pressure depends on the angle from the vertical axis as well as the source-receiver distance. For the simulations considered here and the frequencies of interest, $ka \approx 0.3$ and therefore finite source effects may be significant. Second, material is erupted vertically upwards out of the vent

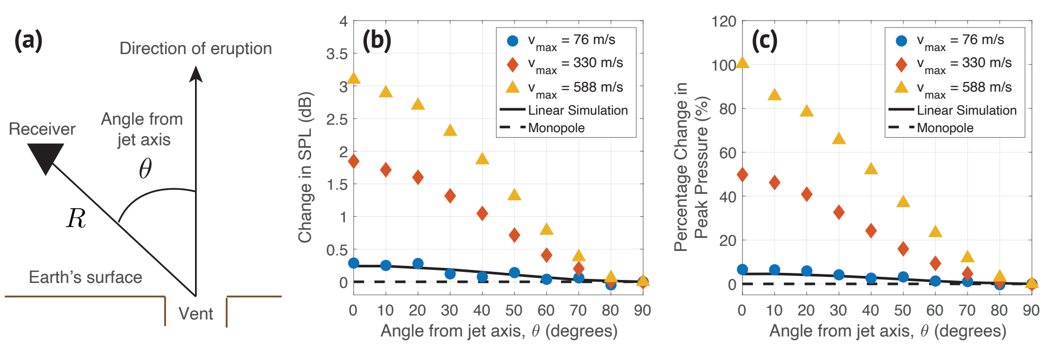

Figure 11. (a) Schematic showing probe location ($R = 1000$ m) and angle from the jet axis, θ. (b) Change in sound pressure level as a function of θ. (c) Percent change in peak pressure as a function of θ. (b) and (c) show the radiation pattern from the nonlinear simulation for three exit velocities; (blue, circles) $v_{\max} = 76$ m/s, (red, diamonds) $v_{\max} = 330$ m/s, and (yellow, triangles) $v_{\max} = 588$ m/s. The black solid line shows the linear simulation while the black dotted line shows the monopole solution.

and is relatively confined between thin shear layers on either side of the vent. This limits the horizontal expansion of the eruptive fluid and subsequent horizontal displacement of the atmospheric air. In contrast, the eruptive fluid expands rapidly in the vertical direction and hence atmospheric air may be preferentially displaced in the vertical direction. Third, the development of vortex rings causes atmospheric air to be pulled towards the vent at the base of the jet. The latter two possible reasons can be grouped together and referred to as jet dynamics.

It is challenging to distinguish between finite source effects and jet dynamics because both of these effects are included in our simulations but not in the compact monopole model. In order to disentangle these two effects, we perform linear acoustic simulations with the same geometry and boundary conditions as shown in Figure 2 using a finite-difference code (Almquist & Dunham, 2020), which we will refer to as the linear simulations. The linear simulations account for finite source effects but do not include the jet dynamics and hence allow these two effects to be distinguished.

The linear simulation results are shown in Figure 11. For the linear simulations the radiation pattern is slightly anisotropic and independent of exit velocity. The sound pressure level recorded above the vent is 0.24 dB greater than on Earth's surface while the peak pressure is 4.5% greater, which is similar to the values for the $v_{\max} = 76$ m/s simulation. This suggests that this small degree of anisotropy is due to finite source effects. For the higher exit velocities, however, the anisotropy is much more pronounced and cannot be explained by finite source effects. Instead, it is likely due to jet dynamics, as we discuss further in Section 5.

5 Discussion

In this section, we explore possible reasons why the nonlinear computational simulations have different waveforms and radiation pattern to the monopole model. We discuss nonlinear propagation, finite source effects, and jet dynamics.

5.1 Nonlinear Propagation Effects

For sonic and supersonic exit velocities, the simulated waveforms have steeper onset and more gradual decay than the monopole solution (Figure 7). Previous work has argued that these N-shaped waveforms can be caused by nonlinear propagation effects (e.g., Marchetti et al., 2013). Here, we investigate the significance of two nonlinear propagation effects: the temperature dependence of the speed of sound and advection of acoustic waves.

The speed of sound is given by

$$c = \sqrt{\gamma Q T}, \tag{14}$$

where γ is the ratio of heat capacities, Q is the specific gas constant, and T is the temperature. Large amplitude pressure waves can compress the atmospheric air, causing adiabatic heating and hence increase the local sound speed. The high temperature parts of the waveform travel faster than the low temperature parts, which results in initially smooth waveforms steepening and forming shockwaves as energy is transferred to higher frequencies (Hamilton & Blackstock, 2008). The dependence of the local sound speed on temperature is a feature of nonlinear acoustics and is in contrast with linear acoustics where the speed of sound is assumed to be constant. We refer to this as the temperature nonlinearity. Anderson (2018) and Maher et al. (2020) invoked the temperature nonlinearity to investigate the asymmetric waveforms (waveforms with a steeper onset and more gradual decay than expected by linear theory) observed in their simulations.

Another important nonlinear effect is advection, where waves propagate at the effective sound speed of $c_{\text{eff}} = \boldsymbol{v} \cdot \hat{\boldsymbol{n}} + c$ where $\boldsymbol{v}$ is the fluid velocity vector and $\hat{\boldsymbol{n}}$ is the normal vector in the direction of wave propagation. This is in contrast with linear acoustics where waves propagate at the background sound speed, c_0, which is independent of fluid velocity. We refer to this as the advection nonlinearity. The background velocity is zero in our simulations (i.e., there is no background wind). Therefore, the velocity that enters in the advection terms is the particle velocity induced by the source and carried by the wave.

We calculate the contributions of these two nonlinear propagation effects to the effective sound speed. The contribution of the temperature and advection nonlinearities are calculated as percentage changes from the background sound speed and are respectively given by:

$$\text{temperature} = \frac{c - c_0}{c_0} \times 100, \tag{15}$$

$$\text{advection} = \frac{\boldsymbol{v} \cdot \hat{\boldsymbol{n}}}{c_0} \times 100. \tag{16}$$

Figure 12 shows a comparison of the two nonlinear effects. Figure 12a-c show the relative contribution of the temperature and advection nonlinearities to the effective sound speed as a function of time for three receiver locations along Earth's surface for eruption simulations with (a) $v_{\max} = 76$ m/s, (b) $v_{\max} = 330$ m/s, and (c) $v_{\max} = 588$ m/s. For both nonlinearities, the amplitude increases with increasing exit velocity. The temperature nonlinearity only causes a small change in the effective sound speed ($< 2\%$). This effect is relatively minor and unlikely to explain the wavefront steepening and shock

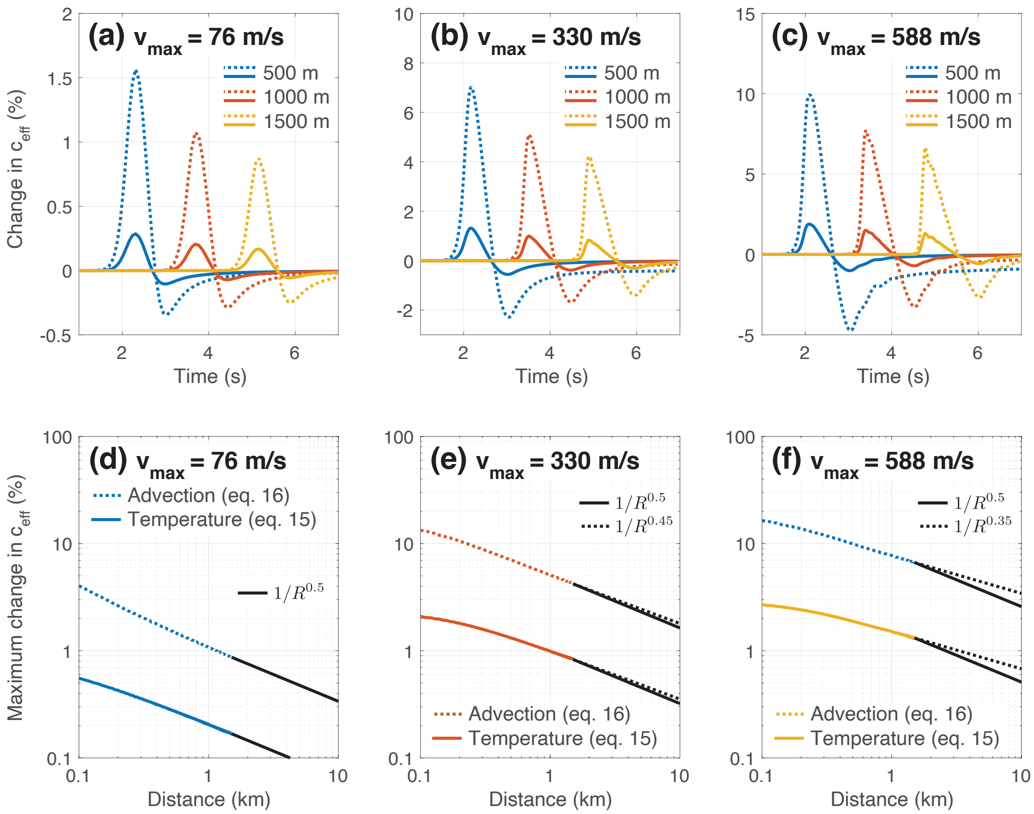

Figure 12. Comparison of advection (dotted, eq. 16) and temperature (solid, eq. 15) nonlinearities for three different maximum exit velocities; (a, d) $v_{\max}$ =76 m/s, (b, e) $v_{\max}$ =330 m/s, and (c, f) $v_{\max}$ =588 m/s. (a, b, and c) Change in effective sound speed as a function of time for three receiver positions along Earth's surface; (blue) 500 m, (red) 1000 m, and (yellow) 1500 m. (d, e, and f) Maximum change in effective sound speed as a function of distance for receivers along Earth's surface. Solid black lines show $1/R^{0.5}$ scaling while dotted black lines show (e) $1/R^{0.45}$ and (f) $1/R^{0.35}$ scaling.

formation as proposed by Anderson (2018) and Maher et al. (2020). The change in effective sound speed caused by the advection nonlinearity is approximately 5 times larger than that caused by the temperature nonlinearity. This shows that the advection is the dominant nonlinearity.

Figure 12d-f show the maximum change in effective sound speed, $\max(c_{\text{eff}})$, caused by the two nonlinearities as a function of distance (from 100 m to 1500 m for the simulation results) for the same three eruption simulations. For all distances considered, the advection nonlinearity dominates. The two nonlinearities have similar trends with distance, suggesting that the advection nonlinearity will dominate at all distances.

We note that our simulations are in 2D and that geometrical spreading is different in 2D and 3D, with particle velocity decaying as $1/\sqrt{R}$ in 2D and $1/R$ in 3D. The temperature perturbation, like the pressure perturbation, decays in the same way as the particle velocity perturbation for linear acoustics. We can use the linear acoustic scaling to anticipate the distance dependence of the advection and temperature nonlinearities. The advection nonlinearity causes a relative change in effective sound speed that is of the order $\boldsymbol{v}/c_0$, and hence proportional to $1/\sqrt{R}$ in 2D and $1/R$ in 3D. The temperature nonlinearity causes a relative change in effective sound speed that is of the order $\Delta T/T_0$, where ΔT is the temperature perturbation and T_0 is the constant background temperature. Because $\boldsymbol{v}$ and ΔT experience the same geometrical spreading, then these two nonlinearities are anticipated to have the same relative importance in 2D and 3D.

The scaling analysis suggests a $1\sqrt{R}$ decay for both nonlinearities in our 2D simulations. This behavior is observed for low exit velocities (Figure 12d), however, as the exit velocity increases the linear scaling analysis breaks down and the two nonlinearities decay at slower than the anticipated $1\sqrt{R}$ rate (Figure 12e,f).

We define that when $\max(c_{\text{eff}}) < 1\%$, then propagation is in the linear regime and nonlinear effects can be neglected. For $v_{\max} = 76$ m/s, $\max(c_{\text{eff}})$ is significantly less than 1% at 10 km distance for both the advection and temperature nonlinearities. For $v_{\max} =$ 330 m/s and $v_{\max} = 588$ m/s, $\max(c_{\text{eff}})$ from the temperature nonlinearity is less than 1% at 10 km distance (0.4% and 0.7% based on $1/R^{0.45}$ and $1/R^{0.35}$ scaling, respectively). For the advection nonlinearity, however, $\max(c_{\text{eff}})$ is greater than 1% at 10 km distance (1.9% and 3.5%, respectively).

The results presented here show that while the temperature nonlinearity does cause a small change in effective sound speed, the advection nonlinearity dominates. While the simulations presented here are limited to a distance of 2 km from the vent, scaling analysis and extrapolation suggests that the advection nonlinearity can be significant at distances of 10 km from the vent for eruptions with high exit velocities (sonic and supersonic). These simulations identify an important nonlinear phenomena that has not been previously discussed in the volcano infrasound literature. The nonlinear propagation effects discussed here can cause observed infrasound waveforms to differ from the waveforms predicted with a linear acoustics framework, such as the compact monopole model as shown in Figure 7. During a volcanic eruption, changes in fluid velocity during the passage of acoustic waves can change the speed of sound, which can lead to wavefront steepening and shock formation. These simulations show that asymmetric waveforms do not necessarily imply large changes in atmospheric temperature and can instead be caused by large fluid velocities, particularly caused by eruptions with high exit velocities. Accounting for these nonlinear effects will provide second-order improvements in accuracy of source parameter estimates compared to the commonly used linear acoustics model of $1/R$ geometrical spreading ($1/\sqrt{R}$ for our 2D simulations). The changes in effective sound speed caused by nonlinear propagation effects, however, are relatively small ($<$ 10%) and in Section 5.3 we examine nonlinear effects in the source region.

5.2 Finite Source Effects

The nonlinear propagation effects discussed above can explain some of the differences between the simulated and monopole waveforms (Figure 7). Nonlinear propagation effects, however, are unable to explain the anisotropic radiation pattern observed in our simulations where the amplitude above the vent is greater than to the side (Figure 11). In this section we consider finite source effects as a possible explanation for the anisotropic radiation pattern. We compare our nonlinear simulations with linear acoustic simulations, which include finite source effects but do not include jet dynamics. This enables us to differentiate between finite source effects and jet dynamics.

Infrasound waveforms for the nonlinear and linear simulations recorded above the vent and on Earth's surface are shown in Figure 13. For $v_{\max} = 76$ m/s, the nonlinear and linear solutions are in reasonable agreement for a receiver on Earth's surface as well as above the vent. This demonstrates that the small amount of anisotropy present in the $v_{\max} = 76$ m/s simulation (peak pressure amplitude is 4.5% larger above the vent than on Earth's surface) can be explained by finite source effects, which are accounted for in the linear simulation. Previous work has modeled infrasound radiation from wide volcanic craters as a baffled piston (Buckingham & Garcés, 1996; Garcés, 2000; Watson

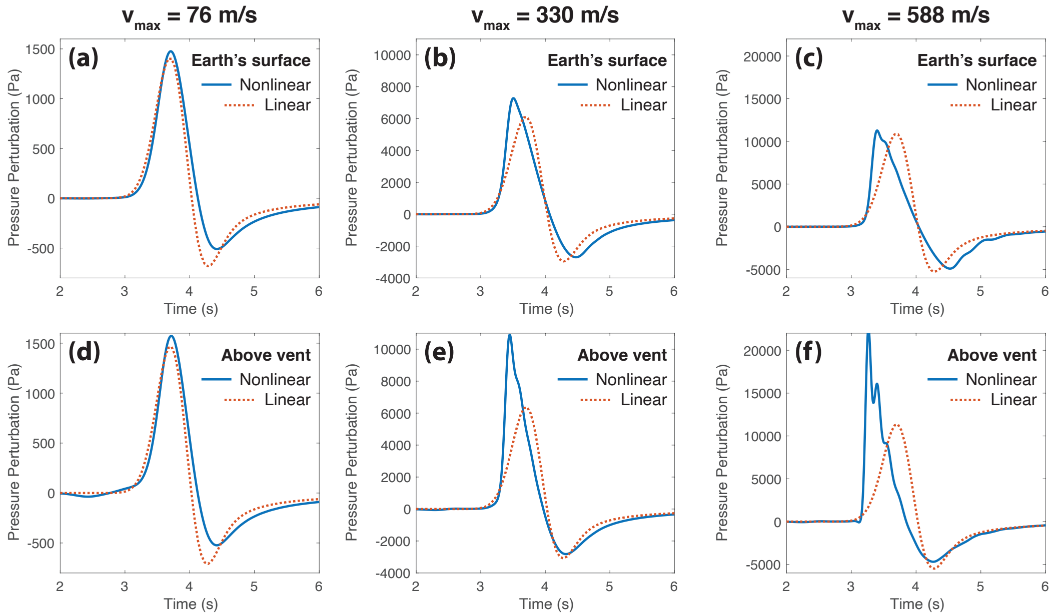

Figure 13. Infrasound waveforms for (blue, solid) nonlinear and (red, dotted) linear simulations for a receiver at (a, b, and c) 1000 m away from the vent on Earth's surface and (d, e, and f) 1000 m vertically above the vent. Three eruption simulations with different maximum exit velocities are shown; (a and d) $v_{\max} = 76$ m/s, (b and e) $v_{\max} = 330$ m/s, and (c and f) $v_{\max} = 588$ m/s.

et al., 2019) where the pressure perturbation in the frequency domain is given by (Rossing & Fletcher, 2004):

$$\Delta p(R, \omega, \theta) = i\omega \exp(-ikR) \frac{\rho_0}{2R\pi a^2} \left[\frac{2J_1(ka \sin\theta)}{ka \sin\theta} \right] V(\omega), \tag{17}$$

where ω is the angular frequency, $k = \omega/c_0$ is the wavenumber, a is the radius of the piston, θ is the angle from the vertical axis to the receiver, and J_1 is a Bessel function of order one. The magnitude of anisotropy observed in our simulations for $v_{\max} = 76$ m/s is in general agreement with the baffled piston solution that predicts the amplitude above the vent will be 10% larger than the amplitude on Earth's surface for $ka = 0.3$, which is the approximate value for the simulations.

The nonlinear and linear simulations diverge as the exit velocity approaches and exceeds the speed of sound with the infrasound signals from the nonlinear simulations having steeper onset and larger amplitudes. The disagreement between the nonlinear and linear simulations is much more pronounced for receivers above the vent than on Earth's surface. For $v_{\max} = 330$ m/s, the nonlinear simulation has a peak amplitude that is 17% larger than the linear simulation for a receiver on Earth's surface but 83% larger for a receiver above the vent. This demonstrates that the large amount of anisotropy present in the $v_{\max} = 330$ m/s and $v_{\max} = 588$ m/s nonlinear simulations (peak pressure amplitude is 50% and 100% larger above the vent than on Earth's surface, respectively) cannot be explained by finite source effects and must be caused by physics that are not included in the linear simulations. Previous observational studies have detected anisotropic infrasound radiation patterns from volcanic eruptions (e.g., Johnson et al., 2008; Jolly et al., 2017; Iezzi et al., 2019) and our simulations provide a theoretical basis for these observations. In the next section, we discuss jet dynamics as a possible explanation for the anisotropy that cannot be explained by finite source effects.

5.3 Jet Dynamics

The fluid dynamics during a volcanic eruption can be extremely complex, particularly in the near-vent region where the pressure, temperature, and fluid velocity are at their highest values. Here, we investigate near-vent fluid dynamics as a possible explanation for (1) why the nonlinear simulations have larger amplitudes and steeper onsets than predicted by the monopole model for high exit velocities and (2) why the nonlinear simulations have much larger amplitudes above the vent than predicted by the monopole model or linear simulations for high exit velocities.

In Section 5.1, we considered the importance of the temperature and advection nonlinearities on the effective wave speed during propagation. We examined receivers at distances > 100 m from the vent and concluded that while the advection nonlinearity dominated both effects were relatively minor during propagation ($< 10\%$ change in effective sound speed). Figure 14 shows the maximum contribution of the temperature and advection nonlinearities in the near-vent region (100 m in the horizontal and 200 m in the vertical) and has the same trends as Figure 12 (advection nonlinearity is larger than temperature and both effects increase with increased exit velocity). However, the advection nonlinearity in the near-vent region is an order of magnitude larger than the advection nonlinearity during propagation. Depending on the exit velocity, the advection nonlinearity in the source region can cause changes in the effective sound speed of up to 170%, which can cause wavefront steepening and shock formation. This suggests that nonlinear effects in the source region near the vent can cause substantial deviations in the waveform shape, amplitude, and arrival time from the predictions of the monopole model, such as shown in Figures 7 and 13. This result suggests that nonlinear effects may be more prevalent in volcanic eruptions than generally assumed. It is much easier to achieve high temperatures and fast fluid velocities close to the vent than far away and hence, as shown

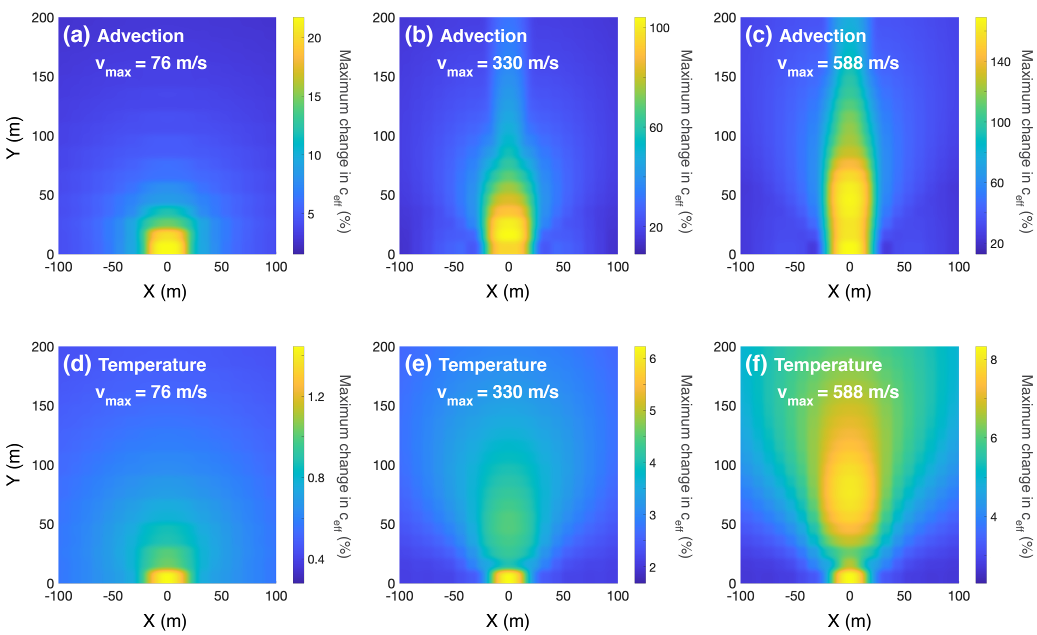

Figure 14. Maximum contribution of advection (top, eq. 16) and temperature (bottom, eq. 15) nonlinearities to the effective speed of sound for eruption simulations with (a, d) $v_{\max} = 76$ m/s, (b, e) $v_{\max} = 330$ m/s, and (c, f) $v_{\max} = 588$ m/s. Note that the scale-bar is an order of magnitude larger for the advection nonlinearity than the temperature nonlinearity.

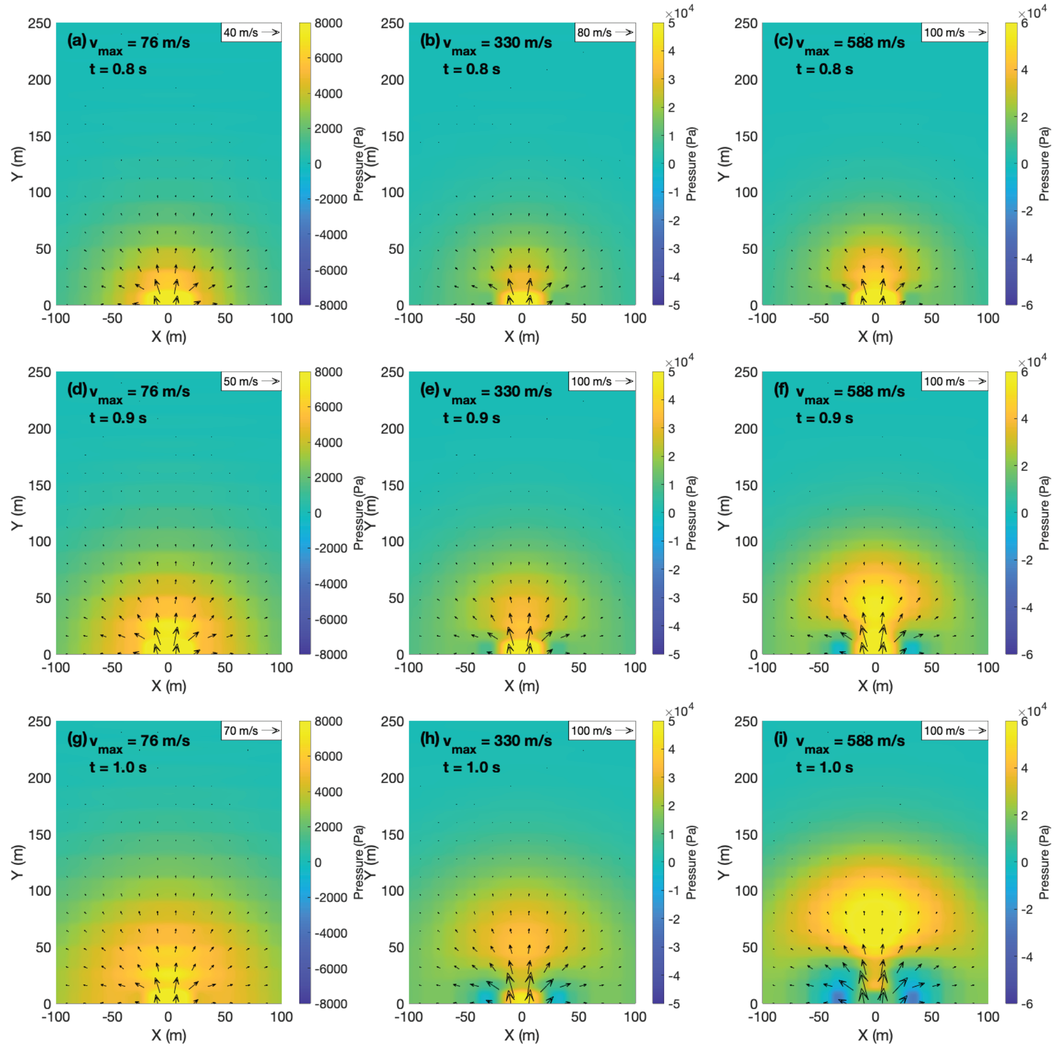

Figure 15. Fluid flow (black arrows) and pressure perturbation (colors) in the near-vent region at $t = 0.8$ s, $t = 0.9$ s, and $t = 1.0$ s for three simulations with different maximum exit velocities.

in the simulations presented here, nonlinear effects are more pronounced near the source than during propagation.

The nonlinear simulations have larger amplitudes above the vent than predicted by the monopole model or linear simulations. In Section 5.2 we showed that the small degree of anisotropy present for low exit velocities (peak amplitude of 4.5% larger above the vent than to the side for $v_{\max} = 76$ m/s) can be explained by finite source effects but the larger degree of anisotropy for the higher exit velocities cannot be (peak amplitude of 50% and 100% larger above the vent than to the side for $v_{\max} = 330$ m/s and $v_{\max} = 588$ m/s, respectively). Here we consider near-vent fluid flow as a possible explanation. Figure 15 shows velocity vectors overlain on the pressure perturbation in the near-vent region for three simulations with different maximum exit velocities. The time snapshots shown in Figure 15 correspond to the approximate source times for acoustic waves recorded at receivers 1000 m from the vent, as shown in Figures 11 and 13.

For $v_{\max} = 76$ m/s, the erupted material expands in all directions and pushes the atmosphere outwards. This results in a radiation pattern that is approximately isotropic (apart from the small amount of anisotropy that was demonstrated in Section 5.2 to be due to finite source effects) and the simulated waveforms are in good agreement with the monopole model for both receivers on Earth's surface and above the vent. The good agreement between the simulated and monopole waveforms coupled with the similar radiation pattern suggests that in this instance the erupted volume is equal to the volume of displaced atmospheric air, which assumed in our application of the monopole model.

For $v_{\max} = 330$ m/s and $v_{\max} = 588$ m/s, the erupted material preferentially expands upwards. Fluid is erupted vertically through the vent. Due to the sharp difference in velocity between the erupted fluid and the stationary atmospheric air, a thin shear layer is created on either side of the vent. This confines the eruptive fluid and inhibits expansion in the horizontal direction. High pressure develops above the vent and low pressure on either side of the vent near Earth's surface. The low pressure on either side of the vent causes the recirculation of fluid back towards the vent, forming vortex rings on either side of the jet. The complex near-vent fluid dynamics shown in Figure 15 results in the infrasound signal recorded above the vent having larger amplitude than that recorded to the side of the vent on Earth's surface. The simulation results presented here demonstrate the near-vent fluid flow can have a significant impact on the observed infrasound signal, especially for eruptions with exit velocities approaching and exceeding the speed of sound where the fluid dynamics are more complex. Further work should continue to link infrasound observations with the complex fluid dynamics observed during volcanic eruptions.

5.4 Future Work

In this work, we perform 2D simulations of idealized volcanic eruptions. Our simulations contain several important simplifications and here we discuss how these simplifications may be addressed in future work.

In our simulations, the erupted material has the same composition and temperature as the atmosphere. For real volcanic eruptions, the erupted material can have a drastically different composition and temperature to the atmosphere as well as contain a significant fraction of solid particles. In particular, a more realistic eruptive fluid would have a much greater heat capacity and density but only slightly greater compressibility, due to rapid heat transfer from particles to the fluid that can buffer against adiabatic temperature changes. As the change in compressibility would be relatively small, the way that the eruptive fluid displaces and compresses the atmospheric air would likely be similar. The higher density of the erupted material, however, would result in greater inertia, which may further amplify the upward radiation relative to the side radiation. Therefore, the radiation pattern for a more realistic erupted fluid could be even more anisotropic than the simulation results presented here. CharLES^X also has the capability to perform 3D simulations, incorporate variable fluid compositions, and simulate particle-laden flows (Mohaddes et al., 2021). These limitations can be addressed in future work to explore the impact of these phenomena on the infrasound signal.

Extensive work over the past decade has demonstrated impact of topography on local infrasound observations through scattering and diffraction (Matoza et al., 2009; Kim & Lees, 2011; Lacanna & Ripepe, 2013; Kim & Lees, 2014; Kim et al., 2015; Fee et al., 2017; Ishii et al., 2020; Lacanna & Ripepe, 2020; Maher et al., 2021). Meteorological conditions and near-vent winds can also strongly impact the observed infrasound signal (Fee & Garcés, 2007; Johnson et al., 2012). In this work, however, we consider flat topography and an initially stationary atmosphere in order to focus on the impact of the exit velocity on the jet dynamics and infrasound signal. Future work could build on these simulations by incorporating local topography, winds, and a stratified atmosphere.

The results presented here demonstrate that nonlinear effects can cause substantial changes in the observed infrasound waveforms, and that inverting nonlinear infrasound signals with linear models can result in underprediction of the erupted volume (Figure 9). The next step is to investigate how these nonlinear effects can be reliably identified in data and be accounted for in processing workflows in order to improve estimates of eruptive source parameters.

Previous modeling work has examined overpressured jets (Ogden, Wohletz, et al., 2008; Ogden, Glatzmaier, & Wohletz, 2008; Koyaguchi et al., 2018). In this work, however, we focus on pressure-balanced jets, where the exit pressure is equal to atmospheric pressure. The jet dynamics in our simulations do not display the complex structures (barrel shocks, standing shocks, Mach disk) observed in overpressured jets (Ogden, Wohletz, et al., 2008; Koyaguchi et al., 2018). As such, this study should be viewed as the simplest possible case of jet dynamics and the associated infrasound signals. We defer a comprehensive study of the infrasound signals of overpressured jets for future work.

We focus on short-duration impulsive explosions that are representative of strombolian and vulcanian eruption styles. Previous work by Matoza et al. (2009) and Matoza et al. (2013) has focused on sustained jet noise, which is likely to occur during sub-plinian and plinian eruptions with sustained eruption columns, and is highly-directional. During these eruptions, sound is likely generated by turbulent structures within the jet (Matoza et al., 2013; Cerminara et al., 2016) rather than the bulk displacement of atmospheric air by the erupted material. There has been extensive work using CharLES^X to model noise from jet engines (Khalighi et al., 2011; Nichols et al., 2012; Brès et al., 2016) and future work could use CharLES^X to model sustained volcanic jetting during sub-plinian and plinian eruptions.

6 Conclusion

Volcanic eruptions frequently generate infrasound signals, however, the relationship between infrasound signals and eruption properties is not well understood. Volcanic eruptions are frequently approximated as monopole sources that radiate linear acoustic waves equally in all directions. There is growing appreciation that volcanic infrasound signals can be influenced by nonlinear propagation and finite source effects, exhibit anisotropic radiation patterns, and are sensitive to the complex fluid dynamics near the vent (Matoza et al., 2013; Iezzi et al., 2019; Maher et al., 2020). In this study, we perform nonlinear computational aeroacoustic simulations of idealized short-duration impulsive volcanic eruptions in two-dimensions in order to better understand the relationship between infrasound observations and eruption properties.

We compare our nonlinear simulation results with the compact monopole source model. For low exit velocities ($v_{\max} < 100$ m/s), infrasound simulations are well described by the monopole model (assuming the source dimension is sufficiently small). As the exit velocity approaches and exceeds the speed of sound, however, the monopole model breaks down. The nonlinear infrasound observations are characterized by sharper onsets, more gradual decay, and lower peak amplitude than predicted by the monopole model. For $v_{\max} = 330$ m/s, the monopole source model underpredicts the slope measured by a receiver on Earth's surface by 53% and overpredicts the peak amplitude by 10%. Interpreting infrasound observations with the linear acoustics framework of the monopole source model can result in substantial underestimation of the erupted volume for eruptions with sonic and supersonic exit velocities (30% lower volume for an eruption with $v_{\max} = 330$ m/s and 37% for $v_{\max} = 588$ m/s).

In addition, the simulated infrasound radiation pattern is anisotropic with larger amplitudes recorded above the vent than to the side on Earth's surface. The degree of anisotropy scales with exit velocity; the peak pressure recorded at the vent is 4.5% larger than on Earth's surface for $v_{\max} = 76$ m/s but 100% larger for $v_{\max} = 588$ m/s. This shows that for eruptions with high exit velocities, ground-based infrasound observations may substantially underpredict the acoustic power of an eruption. The large degree of anisotropy for the high exit velocity eruptions cannot be explained by finite source effects. Instead, it is due to complex fluid dynamics in the near-vent region. The formation of a shear layer on either side of the vent inhibits horizontal expansion and causes the erupted material to preferentially expand upwards, which results in greater pressure amplitudes above the vent than to the side.

Previous work has suggested that the temperature dependence of sound speed could causes wave front steepening and shock formation (Marchetti et al., 2013; Anderson, 2018; Maher et al., 2020). In our simulations, however, the effect of temperature nonlinearity effect is relatively minor. Instead, the advection term (waves travel at the background sound speed plus the local fluid velocity) is the dominant nonlinear propagation effect although this effect only causes sound speed changes on the order of $\sim 10\%$. We are able to examine nonlinear effects in the source region and show that the advection nonlinearity can causes changes in the sound speed of up to $\sim 170\%$ in the near-vent region. This demonstrates that nonlinear source effects are much more significant than propagation effects and future work should focus on improving volcano infrasound source models.

Future work is needed to extend the simulations to 3D, to consider more realistic eruptive compositions and particle concentrations, and to explore the effect of vent overpressure. Nonetheless, this work highlights nonlinear propagation effects, finite source effects, and jet dynamics as important factors to consider when interpreting volcano infrasound observations, especially for eruptions with sonic and supersonic exit velocities. In particular, we demonstrate that near-vent fluid dynamics are extremely important for infrasound generation. Future work should further explore the relationship between the complex near-vent fluid dynamics that are observed during volcanic activity and infrasound observations.

Acknowledgments

The simulation data and analysis code for this work are hosted at the Open Science Framework (doi:10.17605/OSF.IO/2EHUY). We thank the Center for Turbulence Research for providing us with academic access to the CharLES^X modeling code. We thank Robert Clapp for invaluable assistance with installing and running CharLES^X and Martin Almquist for helping with the linear acoustic simulations as well as Robin Matoza and Dorianne Tailpied for their constructive comments during peer-review. This work was supported by National Science Foundation grants EAR-1930979 and EAR-1949219 and benefited from access to the high-performance computing resources provided by Stanford University's Center for Computational Earth and Environmental Sciences.

References

Almquist, M., & Dunham, E. M. (2020). Non-stiff boundary and interface penalties for narrow-stencil finite difference approximations of the Laplacian on curvilinear multiblock grids. *Journal of Computational Physics*, *408*, 109294. Retrieved from `https://doi.org/10.1016/j.jcp.2020.109294` doi: 10.1016/j.jcp.2020.109294

Anderson, J. F. (2018). *Pressure waves and tephra dispersal from volcanic explosions: models, observations, and instrumentation* (Doctoral dissertation, Boise State University). doi: 10.18122/td/1468/boisestate

Arnoult, K. M., Olson, J. V., Szuberla, C. A. L., McNutt, S. R., Garcés, M. A., Fee, D., & Hedlin, M. A. H. (2010). Infrasound observations of the 2008 explosive eruptions of Okmok and Kasatochi volcanoes, Alaska. *Journal of Geophysical Research: Atmospheres*, *115*, 1–12. doi: 10.1029/2010JD013987

Atchley, A. A. (2005). Not your ordinary sound experience: a nonlinear sound primer. *Acoustics Today*, *1*(1), 19–24. Retrieved from `https://acousticstoday.org/not-your-ordinary-sound-experience-a-nonlinear-acoustics-primer-anthony-a-atchley/`

Benage, M. C., Dufek, J., & Mothes, P. A. (2016). Quantifying entrainment in pyroclastic density currents from the Tungurahua eruption, Ecuador: Integrating field proxies with numerical simulations. *Geophysical Research Letters*, *43*(13).

Bercovici, D., & Michaut, C. (2010, 8). Two-phase dynamics of volcanic eruptions: Compaction, compression and the conditions for choking. *Geophysical Journal International*, *182*(2), 843–864. Retrieved from `https://academic.oup.com/gji/article/182/2/843/571789` doi: 10.1111/j.1365-246X.2010.04674.x

Blackstock, D. T. (2000). *Fundamentals of physical acoustics*. Wiley-Interscience.

Brès, G. A., Jaunet, V., Le Rallic, M., Jordan, P., Towne, A., Schmidt, O. T., ... Lele, S. K. (2016). Large eddy simulation for jet noise: azimuthal decomposition and intermittency of the radiated sound. In *Aiaa/ceas aeroacoustics conference* (pp. 1–16). doi: 10.2514/6.2016-3050

Brogi, F., Ripepe, M., & Bonadonna, C. (2018). Lattice Boltzmann modeling to explain volcano acoustic source. *Scientific Reports*(May), 1–8. doi: 10.1038/s41598-018-27387-0

Buckingham, M. J., & Garcés, M. A. (1996). Canonical model of volcano acoustics. *Journal of Geophysical Research*, *101*(B4), 8129–8151.

Bursik, M. I. (1989, 5). Effects of the drag force on the rise height of particles in the gas-thrust region of volcanic eruption columns. *Geophysical Research Letters*, *16*(5), 441–444. Retrieved from `http://doi.wiley.com/10.1029/GL016i005p00441` doi: 10.1029/GL016i005p00441

Bursik, M. I., & Woods, A. W. (1991). Buoyant, superbuoyant and collapsing eruption columns. *Journal of Volcanology and Geothermal Research*, *45*, 347–350.

Caplan-Auerbach, J., Bellesiles, A., & Fernandes, J. K. (2010). Estimates of eruption velocity and plume height from infrasonic recordings of the 2006 eruption of Augustine Volcano, Alaska. *Journal of Volcanology and Geothermal Research*, *189*(1-2), 12–18. doi: 10.1016/j.jvolgeores.2009.10.002

Cerminara, M., Esposti Ongaro, T., & Neri, A. (2016, 10). Large Eddy Simulation of gas–particle kinematic decoupling and turbulent entrainment in volcanic plumes. *Journal of Volcanology and Geothermal Research*, *326*, 143–171. doi: 10.1016/j.jvolgeores.2016.06.018

Chung, W. T., Ma., P. A., & Ihme, M. (2019). Examination of diesel spray combustion in supercritical ambient fluid using large-eddy simulations. *International Journal of Engine Research*, 1–12. doi: 10.1177/1468087419868388

Clarke, A. B., Voight, B., Neri, A., & Macedonio, G. (2002). Transient dynamics of vulcanian explosions and column collapse. *Nature*, *415*(July 1980), 897–901. doi: 10.1038/415897a

Coombs, M. L., Wech, A. G., Haney, M. M., Lyons, J. J., Schneider, D. J., Schwaiger, H. F., ... Tepp, G. (2018). Short-Term Forecasting and Detection of Explosions During the 2016–2017 Eruption of Bogoslof Volcano, Alaska. *Frontiers in Earth Science*, *6*. doi: 10.3389/feart.2018.00122

Courant, R., Friedrichs, K., & Lewy, H. (1967, 4). On the Partial Difference Equations of Mathematical Physics. *IBM Journal of Research and Development*, *11*(2), 215–234. doi: 10.1147/rd.112.0215

De Angelis, S., Diaz-Moreno, A., Zuccarello, L., De Angelis, S., Diaz-Moreno, A., & Zuccarello, L. (2019). Recent Developments and Applications of Acoustic Infrasound to Monitor Volcanic Emissions. *Remote Sensing*, *11*(11), 1302. doi: 10.3390/rs11111302

De Groot-Hedlin, C. D. (2012). Nonlinear synthesis of infrasound propagation through an inhomogeneous, absorbing atmosphere. *Journal of Acoustical Society of America*, *132*. doi: 10.1121/1.4731468

De Groot-Hedlin, C. D. (2016). Long-range propagation of nonlinear infrasound waves through an absorbing atmosphere. *The Journal of the Acoustical Society of America*, *139*, 1565. doi: 10.1121/1.4944759

Dufek, J., & Bergantz, G. W. (2007). Suspended load and bed-load transport of particle-laden gravity currents: The role of particle-bed interaction. *Theoretical and Computational Fluid Dynamics*, *21*(2), 119–145. doi: 10.1007/s00162-007-0041-6

Dufek, J., Manga, M., & Patel, A. (2012). Granular disruption during explosive volcanic eruptions. *Nature Geoscience*, *5*(8), 561–564. doi: 10.1038/ngeo1524

Fee, D., & Garcés, M. (2007). Infrasonic tremor in the diffraction zone. *Geophysical Research Letters*, *34*(16). doi: 10.1029/2007GL030616

Fee, D., Garcés, M., Patrick, M., Chouet, B., Dawson, P., & Swanson, D. (2010). Infrasonic harmonic tremor and degassing bursts from Halema'uma'u Crater, Kilauea Volcano, Hawaii. *Journal of Geophysical Research*, *115*(B11), B11316. doi: 10.1029/2010JB007642

Fee, D., Izbekov, P., Kim, K., Yokoo, A., Lopez, T., Prata, F., ... Iguchi, M. (2017). Eruption mass estimation using infrasound waveform inversion and ash and gas measurements: Evaluation at Sakurajima Volcano, Japan. *Earth and Planetary Science Letters*, *480*, 42–52. doi: 10.1016/J.EPSL.2017.09.043

Fee, D., & Matoza, R. S. (2013). An overview of volcano infrasound: from hawaiian to plinian, local to global. *Journal of Volcanology and Geothermal Research*, 123–137. doi: 10.1016/j.jvolgeores2012.09.002

Garcés, M. A. (2000, 8). Theory of acoustic propagation in a multi-phase stratified liquid flowing within an elastic-walled conduit of varying cross-sectional area. *Journal of Volcanology and Geothermal Research*, *101*(1-2), 1–17. doi: 10.1016/S0377-0273(00)00155-4

Garces, M. A., Fee, D., & Matoza, R. (2013). Volcano acoustics. In S. A. Fagents, T. K. P. Greeg, & R. M. C. Lopes (Eds.), *Modeling volcanic processes: The physics and mathematics of volcanism* (pp. 359–383). Cambridge: Cambridge University Press.

Garnier, E., Adams, N., & Sagaut, P. (2009). *Large eddy simulation for compressible flows.* Springer.

Gaudin, D., Taddeucci, J., Scarlato, P., Moroni, M., Freda, C., Gaeta, M., & Palladino, D. M. (2014, 7). Pyroclast Tracking Velocimetry illuminates bomb ejection and explosion dynamics at Stromboli (Italy) and Yasur (Vanuatu) volcanoes. *Journal of Geophysical Research: Solid Earth*, *119*(7), 5384–5397. Retrieved from `http://www.ov.ingv.it/ov/comunicati-stromboli/comunicato-2009-10-27.pdf].` doi: 10.1002/2014JB011096

Gee, K. L., Sparrow, V. W., Atchley, A., & Gabrielson, T. B. (2007, 3). On the perception of crackle in high-amplitude jet noise. *AIAA Journal*, *45*(3), 593–598. Retrieved from `https://arc.aiaa.org/doi/abs/10.2514/1.26484` doi: 10

.2514/1.26484

Gee, K. L., Sparrow, V. W., James, M. M., Downing, J. M., Hobbs, C. M., Gabrielson, T. B., & Atchley, A. A. (2008). The role of nonlinear effects in the propagation of noise from high-power jet aircraft. *Journal of the Acoustical Society of America*, *123*, 4082. doi: 10.1121/1.2903871

Goodwin, D., Speth, R., Moffat, H., & Weber, B. (2018). *Cantera: An object-oriented software toolkit for chemical kinetics, thermodynamics, and transport processes.* Retrieved from `https://www.cantera.org/` doi: 10.5281/zenodo.1174508

Hamilton, M. F., & Blackstock, D. T. (2008). *Nonlinear acoustics.* Melville, New York: Academic Press.

Hickey, J.-P., & Ihme, M. (2014). Large Eddy Simulation of Supercritical Mixing and Combustion for Rocket Applications. *52nd Aerospace Sciences Meeting*(January), 1–13. doi: 10.2514/6.2014-0138

Iezzi, A. M., Fee, D., Kim, K., Jolly, A. D., & Matoza, R. S. (2019). Three-Dimensional Acoustic Multipole Waveform Inversion at Yasur Volcano, Vanuatu. *Journal of Geophysical Research: Solid Earth*, 2018JB017073. doi: 10.1029/2018JB017073

Ishihara, K. (1985). Dynamical analysis of volcanic explosion. *Journal of Geodynamics*, *3*(3-4), 327–349. doi: 10.1016/0264-3707(85)90041-9

Ishii, K., Yokoo, A., Iguchi, M., & Fujita, E. (2020, 9). Utilizing the solution of sound diffraction by a thin screen to evaluate infrasound waves attenuated around volcano topography. *Journal of Volcanology and Geothermal Research*, *402*, 106983. doi: 10.1016/j.jvolgeores.2020.106983

Jaravel, T., Labahn, J., Sforzo, B., Seitzman, J., & Ihme, M. (2019). Numerical study of the ignition behavior of a post-discharge kernel in a turbulent stratified crossflow. *Proceedings of the Combustion Institute*, *37*, 5065–5072. doi: 10.1016/j.proci.2018.06.226

Johnson, J. B. (2018, 10). Local volcano infrasound monitoring. In *Infrasound monitoring for atmospheric studies: Challenges in middle atmosphere dynamics and societal benefits: Second edition* (pp. 989–1022). Springer International Publishing. Retrieved from `https://doi.org/10.1007/978-3-319-75140-5_32` doi: 10.1007/978-3-319-75140-5{_}32

Johnson, J. B., Anderson, J., Marcillo, O., & Arrowsmith, S. (2012). Probing local wind and temperature structure using infrasound from Volcan Villarrica (Chile). *Journal of Geophysical Research*, *117*. doi: 10.1029/2012JD017694

Johnson, J. B., Aster, R., Jones, K. R., & McIntosh, B. (2008). Acoustic source characterization of impulsive Strombolian eruptions from the Mount Erebus lava lake. *Journal of Volcanology and Geothermal Research*, *177*(3), 673–686. doi: 10.1016/J.JVOLGEORES.2008.06.028

Johnson, J. B., & Miller, A. J. C. (2014). Application of the Monopole Source to Quantify Explosive Flux during Vulcanian Explosions at Sakurajima Volcano (Japan). *Seismological Research Letters*, *85*(6), 1163–1176. doi: 10.1785/0220140058

Johnson, J. B., & Ripepe, M. (2011). Volcano infrasound: A review. *Journal of Volcanology and Geothermal Research*, *206*(3-4), 61–69. doi: 10.1016/j.jvolgeores.2011.06.006

Johnson, J. B., Watson, L. M., Palma, J. L., Dunham, E. M., & Anderson, J. F. (2018). Forecasting the eruption of an open-vent volcano using resonant infrasound tones. *Geophysical Research Letters*, 1–8. doi: 10.1002/2017GL076506

Jolly, A. D., Matoza, R. S., Fee, D., Kennedy, B. M., Iezzi, A. M., Fitzgerald, R. H., . . . Johnson, R. (2017). Capturing the Acoustic Radiation Pattern of Strombolian Eruptions using Infrasound Sensors Aboard a Tethered Aerostat, Yasur Volcano, Vanuatu. *Geophysical Research Letters*, *44*(19), 9672–9680. doi: 10.1002/2017GL074971

Khalighi, Y., Ham, F., Nichols, J., Lele, S., & Moin, P. (2011). Unstructured Large Eddy Simulation for Prediction of Noise Issued from Turbulent Jets in Various Configurations. *17th AIAA/CEAS Aeroacoustics Conference (32nd AIAA Aeroacoustics Conference)*(June), 5–8. doi: 10.2514/6.2011-2886

Kim, K., Fee, D., Yokoo, A., & Lees, J. M. (2015). Acoustic source inversion to estimate volume flux from volcanic explosions. *Geophysical Research Letters*, *42*(13), 5243–5249. doi: 10.1002/2015GL064466

Kim, K., & Lees, J. M. (2011). Finite-difference time-domain modeling of transient infrasonic wavefields excited by volcanic explosions. *Geophysical Research Letters*, *38*(L06804). doi: 10.1029/2010GL046615

Kim, K., & Lees, J. M. (2014). Local Volcano Infrasound and Source Localization Investigated by 3D Simulation. *Seismological Research Letters*, *85*(6), 1177–1186. doi: 10.1785/0220140029

Kim, K., Lees, J. M., & Ruiz, M. (2012). Acoustic multipole source model for volcanic explosions and inversion for source parameters. *Geophysical Journal International*, 1192–1204. doi: 10.1111/j.1365-246X.2012.05696.x

Koyaguchi, T., & Suzuki, Y. J. (2018). The Condition of Eruption Column Collapse: 1. A Reference Model Based on Analytical Solutions. *Journal of Geophysical Research: Solid Earth*, *123*(9), 7461–7482. doi: 10.1029/2017JB015308

Koyaguchi, T., Suzuki, Y. J., & Kozono, T. (2010). Effects of the crater on eruption column dynamics. *Journal of Geophysical Research*, *115*(B7), B07205. doi: 10.1029/2009JB007146

Koyaguchi, T., Suzuki, Y. J., Takeda, K., & Inagawa, S. (2018). The Condition of Eruption Column Collapse: 2. Three-Dimensional Numerical Simulations of Eruption Column Dynamics. *Journal of Geophysical Research: Solid Earth*, *123*(9), 7483–7508. doi: 10.1029/2017JB015259

Lacanna, G., Ichihara, M., Iwakuni, M., Takeo, M., Iguchi, M., & Ripepe, M. (2014, 4). Influence of atmospheric structure and topography on infrasonic wave propagation. *Journal of Geophysical Research: Solid Earth*, *119*(4), 2988–3005. Retrieved from `https://agupubs.onlinelibrary.wiley.com/doi/full/10.1002/2013JB010827https://agupubs.onlinelibrary.wiley.com/doi/abs/10.1002/2013JB010827https://agupubs.onlinelibrary.wiley.com/doi/10.1002/2013JB010827` doi: 10.1002/2013JB010827

Lacanna, G., & Ripepe, M. (2013, 1). Influence of near-source volcano topography on the acoustic wavefield and implication for source modeling. *Journal of Volcanology and Geothermal Research*, *250*, 9–18. doi: 10.1016/j.jvolgeores.2012.10.005

Lacanna, G., & Ripepe, M. (2020, 6). Modeling the Acoustic Flux Inside the Magmatic Conduit by 3D-FDTD Simulation. *Journal of Geophysical Research: Solid Earth*, *125*(6), e2019JB018849. Retrieved from `https://doi.org/` doi: 10.1029/2019JB018849

Lamb, O. D., De Angelis, S., & Lavallée, Y. (2015, 12). Using infrasound to constrain ash plume rise. *Journal of Applied Volcanology*, *4*(1), 1–9. Retrieved from `https://link.springer.com/articles/10.1186/s13617-015-0038-6https://link.springer.com/article/10.1186/s13617-015-0038-6` doi: 10.1186/s13617-015-0038-6

Lele, S. K. (1997). Computational aeroacoustics - A review. *AIAA Meeting Papers on Disc*(January), 1–15. doi: doi:10.2514/6.1997-18

Lighthill, M. J. (1952). On sound generated aerodynamically: I. General theory. *Proc. Roy. Soc. London Ser. A*, *211*, 564–587.

Lyrintzis, A. S., & Coderoni, M. (2019). The use of large eddy simulations in jet aeroacoustics. In *Aiaa scitech 2019 forum.* American Institute of Aeronautics and Astronautics Inc, AIAA. doi: 10.2514/6.2019-0633

Ma, P. C., Wu, H., Jaravel, T., Bravo, L., & Ihme, M. (2018). Large-eddy simulations of transcritical injection and auto-ignition using diffuse-interface method and finite-rate chemistry. *Proceedings of the Combustion Institute*, *000*, 1–8. doi: 10.1016/j.proci.2018.05.063

Ma, P. C., Wu, H., Labahn, J. W., Jaravel, T., & Ihme, M. (2019). Analysis of transient blow-out dynamics in a swirl-stabilized combustor using large-eddy simulations. *Proceedings of the Combustion Institute*, *37*, 5073–5082. doi: 10.1016/j.proci.2018.06.066

Maher, S. P., Matoza, R., de Groot-Hedlin, C., Jolly, A., Gee, K., & Fee, D. (2019). Investigating the Effect of Nonlinear Acoustic Propagation on Infrasound-Based Volume Flux Estimates at Yasur Volcano, Vanuatu. In *American geophysical union fall meeting.*

Maher, S. P., Matoza, R., de Groot-Hedlin, C., Kim, K., & Gee, K. (2021). Evaluating the applicability of a screen diffraction approximation to local volcano infrasound. *Volcanica*, 67–85. doi: 10.30909/vol.04.01.6785

Maher, S. P., Matoza, R. S., Groot-Hedlin, C. D., Gee, K. L., Fee, D., & Yokoo, A. (2020, 3). Investigating Spectral Distortion of Local Volcano Infrasound by Nonlinear Propagation at Sakurajima Volcano, Japan. *Journal of Geophysical Research: Solid Earth*, *125*(3). Retrieved from `https://onlinelibrary.wiley.com/doi/10.1029/2019JB018284` doi: 10.1029/2019JB018284

Marchetti, E., Ripepe, M., Campus, P., Le Pichon, A., Brachet, N., Blanc, E., ... Arnal, T. (2019, 10). Infrasound monitoring of volcanic eruptions and contribution of ARISE to the volcanic ash advisory centers. In *Infrasound monitoring for atmospheric studies: Challenges in middle atmosphere dynamics and societal benefits: Second edition* (pp. 1141–1162). Springer International Publishing. Retrieved from `https://doi.org/10.1007/978-3-319-75140-5_36` doi: 10.1007/978-3-319-75140-5{_}36

Marchetti, E., Ripepe, M., Delle Donne, D., Genco, R., Finizola, A., & Garaebiti, E. (2013). Blast waves from violent explosive activity at Yasur Volcano, Vanuatu. *Geophysical Research Letters*, *40*(22), 5838–5843. doi: 10.1002/2013GL057900

Matoza, R. S., Fee, D., Garcés, M. A., Seiner, J. M., Ramón, P. A., & Hedlin, M. A. (2009). Infrasonic jet noise from volcanic eruptions. *Geophysical Research Letters*, *36*(8). doi: 10.1029/2008GL036486

Matoza, R. S., Fee, D., Green, D., & Mialle, P. (2019, 10). Volcano infrasound and the international monitoring system. In *Infrasound monitoring for atmospheric studies: Challenges in middle atmosphere dynamics and societal benefits: Second edition* (pp. 1023–1077). Springer International Publishing. Retrieved from `https://doi.org/10.1007/978-3-319-75140-5_33` doi: 10.1007/978-3-319-75140-5{_}33

Matoza, R. S., Fee, D., & López, T. M. (2014, 11). Acoustic characterization of explosion complexity at Sakurajima, Karymsky, and Tungurahua volcanoes. *Seismological Research Letters*, *85*(6), 1187–1199. Retrieved from `http://pubs.geoscienceworld.org/ssa/srl/article-pdf/85/6/1187/2768758/1187.pdf` doi: 10.1785/0220140110

Matoza, R. S., Fee, D., Neilsen, T. B., Gee, K. L., & Ogden, D. E. (2013). Aeroacoustics of volcanic jets: Acoustic power estimation and jet velocity dependence. *J. Geophys. Res. Solid Earth*, *118*, 6269–6284. doi: 10.1002/2013JB010303

Matoza, R. S., Hedlin, M. A., & Garcés, M. A. (2007). An infrasound array study of Mount St. Helens. *Journal of Volcanology and Geothermal Research*, *160*(3-4), 249–262. doi: 10.1016/j.jvolgeores.2006.10.006

McKee, K., Fee, D., Yokoo, A., Matoza, R. S., & Kim, K. (2017). Analysis of gas jetting and fumarole acoustics at Aso Volcano, Japan. *Journal of Volcanology and Geothermal Research*, *340*, 16–29. doi: 10.1016/J.JVOLGEORES.2017.03.029

Medici, E. F., Allen, J. S., & Waite, G. P. (2014). Modeling shock waves generated by explosive volcanic eruptions. *Geophysical Research Letters*, *41*(2), 414–421. doi: 10.1002/2013GL058340

Mohaddes, D., Xie, W., & Ihme, M. (2021). Analysis of low-temperature chemistry in a turbulent swirling spray flame near lean blow-out. *Proceedings of the Combustion Institute*, *38*.

Neri, A., Esposti Ongaro, T., Macedonio, G., & Gidaspow, D. (2003). Multiparticle simulation of collapsing volcanic columns and pyroclastic flow. *Journal of Geophysical Research: Solid Earth*, *108*(B4), 2202. Retrieved from `http://dx.doi.org/10.1029/2001JB000508` doi: 10.1029/2001JB000508

Neri, A., & Macedonio, G. (1996, 4). Numerical simulation of collapsing volcanic columns with particles of two sizes. *Journal of Geophysical Research: Solid Earth*, *101*(B4), 8153–8174. Retrieved from `http://doi.wiley.com/10.1029/95JB03451` doi: 10.1029/95JB03451

Nichols, J. W., Lele, S. K., Moin, P., Ham, F. E., & Bridges, J. E. (2012). Large-eddy simulation for supersonic rectangular jet noise prediction: Effects of chevrons. In *18th aiaa/ceas aeroacoustics conference (33rd aiaa aeroacoustics conference).* doi: 10.2514/6.2012-2212

Nordström, J., & Svärd, M. (2005). Well-posed boundary conditions for the Navier-Stokes equations. *SIAM Journal on Numerical Analysis*, *43*(3), 1231–1255. doi: 10.1137/040604972

Ogden, D. E. (2011, 12). Fluid dynamics in explosive volcanic vents and craters. *Earth and Planetary Science Letters*, *312*(3-4), 401–410. doi: 10.1016/j.epsl.2011.10.032

Ogden, D. E., Glatzmaier, G. A., & Wohletz, K. H. (2008, 4). Effects of vent overpressure on buoyant eruption columns: Implications for plume stability. *Earth and Planetary Science Letters*, *268*(3-4), 283–292. doi: 10.1016/j.epsl.2008.01.014

Ogden, D. E., Wohletz, K. H., Glatzmaier, G. A., & Brodsky, E. E. (2008). Numerical simulations of volcanic jets: Importance of vent overpressure. *Journal of Geophysical Research: Solid Earth*, *113*(2), 1–18. doi: 10.1029/2007JB005133

Peña Fernández, J. J., Cigala, V., Kueppers, U., & Sesterhenn, J. (2020, 12). Acoustic analysis of starting jets in an anechoic chamber: implications for volcano monitoring. *Scientific Reports*, *10*(1), 1–12. Retrieved from `https://doi.org/10.1038/s41598-020-69949-1` doi: 10.1038/s41598-020-69949-1

Perttu, A., Taisne, B., De Angelis, S., Assink, J. D., Tailpied, D., & Williams, R. A. (2020, 9). Estimates of plume height from infrasound for regional volcano monitoring. *Journal of Volcanology and Geothermal Research*, *402*, 106997. doi: 10.1016/j.jvolgeores.2020.106997

Poinsot, T. J., & Lelef, S. K. (1992). Boundary conditions for direct simulations of compressible viscous flows. *Journal of Computational Physics*, *101*(1), 104–129. doi: 10.1016/0021-9991(92)90046-2

Pope, S. B. (2001). *Turbulent Flows* (Vol. 12) (No. 11). IOP Publishing. Retrieved from `https://iopscience.iop.org/article/10.1088/0957-0233/12/11/705` doi: 10.1088/0957-0233/12/11/705

Richardson, J. P., Waite, G. P., & Palma, J. L. (2014). Varying seismic-acoustic properties of the fluctuating lava lake at Villarrica volcano, Chile. *Journal of Geophysical Research: Solid Earth*, 1–14. doi: 10.1002/2014JB011002.Received

Ripepe, M., Marchetti, E., Delle Donne, D., Genco, R., Innocenti, L., Lacanna, G., & Valade, S. (2018). Infrasonic Early Warning System for Explosive Eruptions. *Journal of Geophysical Research: Solid Earth*, *123*(11), 9570–9585. doi: 10.1029/2018JB015561

Rossing, T. D., & Fletcher, N. H. (2004). *Principles of Vibration and Sound* (Second ed., Vol. 1). Springer. doi: 10.1017/CBO9781107415324.004

Rowell, C. R., Fee, D., Szuberla, C. A., Arnoult, K., Matoza, R. S., Firstov, P. P., … Makhmudov, E. (2014). Three-dimensional volcano-acoustic source localization at Karymsky Volcano, Kamchatka, Russia. *Journal of Volcanology and Geothermal Research*, *283*, 101–115. doi: 10.1016/J.JVOLGEORES.2014.06.015

Shariff, K., & Leonard, A. (1992). Vortex Rings. *Annu. Rev. Fluid Mech. 1992*, *24*, 235–279. doi: 10.1146/annurev.fl.24.010192.001315

Sparks, R., & Wilson, L. (1976). A model for the formation of ignimbrite by gravitational column collapse. *Journal of the Geological Society*, *132*(4), 441–451. doi: 10.1144/gsjgs.132.4.0441

Suzuki, Y. J., & Koyaguchi, T. (2012, 4). 3-D numerical simulations of eruption column collapse: Effects of vent size on pressure-balanced jet/plumes. *Journal of Volcanology and Geothermal Research*, *221-222*, 1–13. doi: 10.1016/j.jvolgeores.2012.01.013

Svärd, M., Carpenter, M. H., & Nordström, J. (2007). A stable high-order finite difference scheme for the compressible Navier-Stokes equations, far-field boundary conditions. *Journal of Computational Physics*, *225*(1), 1020–1038. doi: 10.1016/j.jcp.2007.01.023

Swanson, E., Theunissen, R., Rust, A., Green, D., & Phillips, J. (2018, 9). An experimental study of the flow structure and acoustics of jets: Implications for volcano infrasound. *Journal of Volcanology and Geothermal Research*, *363*, 10–22. doi: 10.1016/j.jvolgeores.2018.08.005

Taddeucci, J., Alatorre-Ibarguengoitia, M. A., Palladino, D. M., Scarlato, P., & Camaldo, C. (2015). High-speed imaging of Strombolian eruptions: Gas-pyroclast dynamics in initial volcanic jets. *Geophysical Research Letters*, *42*(15), 6253–6260. doi: 10.1002/2015GL064874

Taddeucci, J., Scarlato, P., Capponi, A., Del Bello, E., Cimarelli, C., Palladino, D. M., & Kueppers, U. (2012). High-speed imaging of Strombolian explosions: The ejection velocity of pyroclasts. *Geophysical Research Letters*, *39*(2). doi: 10.1029/2011GL050404

Taddeucci, J., Sesterhenn, J., Scarlato, P., Stampka, K., Del Bello, E., Pena Fernandez, J., & Gaudin, D. (2014). High-speed imaging, acoustic features, and aeroacoustic computations of jet noise from Strombolian (and Vulcanian) explosions. *Geophysical Research Letters*, *41*, 3096–3102. doi: 10.1002/2014GL059925.Received

Tam, C. K. (1998). Jet noise: Since 1952. *Theoretical and Computational Fluid Dynamics*, *10*(1-4), 393–405. Retrieved from `https://link.springer.com/article/10.1007/s001620050072` doi: 10.1007/s001620050072

Tam, C. K., & Webb, J. C. (1993, 8). Dispersion-relation-preserving finite difference schemes for computational acoustics. *Journal of Computational Physics*, *107*(2), 262–281. doi: 10.1006/jcph.1993.1142

Vergniolle, S., & Brandeis, G. (1996). Strombolian explosions: 1. A large bubble breaking at the surface of a lava column as a source of sound. *Journal of Geophysical Research*, *101*(B9), 20433. doi: 10.1029/96JB01178

Vreman, A. W. (2004). An eddy-viscosity subgrid-scale model for turbulent shear flow: Algebraic theory and applications. *Physics of Fluids*, *16*(10), 3670–3681. doi: 10.1063/1.1785131

Watson, L. M., Dunham, E. M., & Johnson, J. B. (2019). Simulation and inversion of harmonic infrasound from open-vent volcanoes using an efficient quasi-1D crater model. *Journal of Volcanology and Geothermal Research*, *380*, 64–79. doi: 10.1016/j.jvolgeores.2019.05.007

Watson, L. M., Johnson, J. B., Sciotto, M., & Cannata, A. (2020). Changes in crater geometry revealed by inversion of harmonic infrasound observations : 24 December 2018 eruption of Mount Etna , Italy. *Geophysical Research Letters*.

Wilson, L. (1976). Explosive Volcanic Eruptions-111. Plinian Eruption Columns.

Geophys. J.R. Astr. Soc., *45*, 543–556. Retrieved from https://academic.oup.com/gji/article/45/3/543/690542 doi: 10.1111/j.1365-246X.1976.tb06909.x

Wilson, L., Sparks, R. S. J., Huang, T. C., & Watkins, N. D. (1978). The control of volcanic column heights by eruption energetics and dynamics. *Journal of Geophysical Research: Solid Earth*, *83*(B4), 1829–1836. Retrieved from http://dx.doi.org/10.1029/JB083iB04p01829 doi: 10.1029/JB083iB04p01829

Wilson, L., Sparks, S. J., & Walker, L. (1980). Explosive volcanic eruptions - IV: the control of magma properties and conduit geometry on eruption column behaviour. *Geophys. J.R. Astr. Soc.*, *63*, 117–148.

Witsil, A. J., & Johnson, J. B. (2018). Infrasound explosion and coda signal investigated with joint analysis of video at Mount Erebus, Antarctica. *Journal of Volcanology and Geothermal Research*, *357*, 306–320. doi: 10.1016/j.jvolgeores.2018.05.002

Woods, A. W. (1988). The fluid dynamics and thermo dynamics of eruption columns. *Bulletin of Volcanology*, *50*, 169–193. doi: 10.1007/BF01079681

Woulff, G., & McGetchin, T. R. (1976). Acoustic noise from volcanoes - Theory and experiment. *Geophysical Journal of the Royal Astronomical Society*, *45*, 601–616. doi: 10.1111/j.1365-246X.1976.tb06913.x

Yamada, T., Aoyama, H., Nishimura, T., Iguchi, M., & Hendrasto, M. (2017). Volcanic eruption volume flux estimations from very long period infrasound signals. *Geophysical Research Letters*, *44*(1), 143–151. doi: 10.1002/2016GL071047

Yarushina, V. M., Bercovici, D., & Michaut, C. (2015, 3). Two-phase dynamics of volcanic eruptions: Particle size distribution and the conditions for choking. *Journal of Geophysical Research: Solid Earth*, *120*(3), 1503–1522. Retrieved from https://agupubs.onlinelibrary.wiley.com/doi/full/10.1002/2014JB011195https://agupubs.onlinelibrary.wiley.com/doi/abs/10.1002/2014JB011195https://agupubs.onlinelibrary.wiley.com/doi/10.1002/2014JB011195 doi: 10.1002/2014JB011195

Yokoo, A., & Ishihara, K. (2007). Analysis of pressure waves observed in Sakurajima eruption movies. *Earth, Planets and Space*(2004), 177–181.